

Optical constraints on the coldest metal-poor population

J.-Y. Zhang^{1,2,3,*}, N. Lodieu^{1,2}, E. L. Martín^{1,2}, M. R. Zapatero Osorio⁴, V. J. S. Béjar^{1,2}, V. D. Ivanov³, H. M. J. Boffin³, T. Shahbaz^{1,2}, Ya. V. Pavlenko^{5,1}, R. Rebolo^{1,2}, B. Gauza⁶, N. Sedighi^{1,2}, and C. Quezada^{7,8,3}

¹ Instituto de Astrofísica de Canarias (IAC), Calle Vía Láctea s/n, E-38200 La Laguna, Tenerife, Spain

² Departamento de Astrofísica, Universidad de La Laguna (ULL), E-38206 La Laguna, Tenerife, Spain

³ European Southern Observatory, Karl-Schwarzschild-Str. 2, 85748 Garching bei München, Germany

⁴ Centro de Astrobiología (CAB), CSIC-INTA, Camino Bajo del Castillo s/n, 28692 Villanueva de la Cañada, Madrid, Spain

⁵ Main Astronomical Observatory, Academy of Sciences of the Ukraine, 27 Zabolotnoho, Kyiv 03143, Ukraine

⁶ Janusz Gil Institute of Astronomy, University of Zielona Góra, Lubuska 2, 65-265 Zielona Góra, Poland

⁷ Instituto de Astrofísica, Pontificia Universidad Católica de Chile, Av. Vicuña Mackenna 4860, 782-0436 Macul, Santiago, Chile

⁸ Millennium Institute of Astrophysics, Av. Vicuña Mackenna 4860, 82-0436 Macul, Santiago, Chile

December 6, 2024, December 6, 2024

ABSTRACT

Context. The coldest metal-poor population made of T and Y dwarfs are archaeological tracers of our Galaxy because they are very old and have kept the pristine material. The optical properties of these objects are important to characterise their atmospheric properties.

Aims. We aim at characterising further the optical properties of ultracool metal-poor population with deep far-red optical images and parallax determinations.

Methods. We collected deep optical imaging of 12 metal-poor T dwarf candidates and the only potential metal-poor Y dwarf, a.k.a., the Accident using the 10.4-m Gran Telescopio Canarias, the 8.2-m European Southern Observatory Very Large Telescope, and the Dark Energy Survey. We have been monitoring the positions of five metal-poor T dwarf candidates using Calar-Alto 3.5-m telescope for two years to infer their distances. We compared these objects with solar-metallicity dwarfs in colour-magnitude and colour-colour diagrams as well as with state-of-the-art theoretical ultracool models.

Results. We solve trigonometric parallaxes of the five metal-poor T dwarf candidates. We obtain z' -band photometry for the other 12 metal-poor T dwarf candidates, increasing the sample of T subdwarfs with optical photometry from 12 to 24. We report a 3- σ limit for the Accident in five optical bands. We confirm four T subdwarfs and the Accident as a Y subdwarf, and propose two more Y subdwarf candidates. We emphasise that the $z_{PS1} - W1$ colour combining with the $W1 - W2$ colour could break the metallicity-temperature degeneracy for T and possibly for Y dwarfs. The $z_{PS1} - W1$ colour shifts redward when metallicity decreases for a certain temperature, which is not predicted by models. The Accident has the reddest $z_{PS1} - W1$ colour among our sample. The $z_{PS1} - W1$ colour will be useful to search for other examples of this cold and old population in upcoming and existing deep optical and infrared large-area surveys.

1. Introduction

Substellar objects formed at early times of our Milky Way are valuable tracers of the original chemical composition of our Galaxy. With masses below the hydrogen burning limit, which ranges from $0.075M_{\odot}$ for solar metallicity (Chabrier et al. 2023) to $0.092M_{\odot}$ for zero metallicity (Saumon et al. 1994), they could not establish a stable hydrogen fusion and, thus, they retain most of their pristine metal-poor material. Due to their old age, they have emitted away most of their gravitational contraction energy. They have been cooling down to extremely low temperatures, and hence have very late spectral types: T type (Burgasser et al. 2002, 2003b) and Y type (Delorme et al. 2008; Cushing et al. 2011). They normally possess high proper motions and high radial velocities, which are typical kinematics associated with the halo or the thick-disk population of our Milky Way (Gizis et al. 1997; Zhang et al. 2017).

Since the first two unambiguous brown dwarfs, Teide 1 and Gliese 229B, were discovered three decades ago (Rebolo et al. 1995; Nakajima et al. 1995), thousands of substellar objects with a wide range of properties have been found. On the other hand, the first metal-poor brown dwarfs, or subdwarfs, were an-

nounced eight years later with the discovery of the first L subdwarf (Burgasser et al. 2003a). Later on, dozens of L subdwarfs have been found and classified (Sivarani et al. 2009; Cushing et al. 2009; Burgasser et al. 2009; Lodieu et al. 2010; Kirkpatrick et al. 2014; Zhang et al. 2017, 2018). Few metal-poor T dwarf candidates have been revealed in the last ten years (Murray et al. 2011; Mace et al. 2013b; Pinfield et al. 2014; Burningham et al. 2014; Kellogg et al. 2018; Schneider et al. 2020; Greco et al. 2019; Meisner et al. 2020b, 2021; Schneider et al. 2021; Brooks et al. 2022). The classification of the T subdwarf population is still under development. The only metal-poor Y dwarf candidate to date, known as 'the Accident', was announced just recently by Kirkpatrick et al. (2021b).

Most cold substellar objects, whether metal-poor or not, are primarily characterised in the infrared (IR) wavelengths where their spectral energy distributions peak, in accordance with their temperatures and Planck's radiation law. Our previous work (Zhang et al. 2023) demonstrates that the far-red optical window can provide a unique window for constraining the metallicity of this cold population, while Martín et al. (2024) shows that the coldest population of Y dwarfs are actually brighter in the optical than what models predict.

* e-mail: jzhang@iac.es

Table 1: List of metal-poor T and Y dwarf candidates in our work separated by astrometric and photometric samples. They are ordered by right ascension. The coordinates are in degrees under equinox J2000. MJDs are the Modified Julian dates of these coordinates. $\text{MJD} = \text{JD} - 2500000.5$. If not specified, all the information is from the same references as those of the targets. In the rest of the paper, we subsequently use *Whmm* as abbreviations for these objects.

For astrometry:

Full name	α, δ (deg)	MJD	$\mu_{\alpha \cos \delta}, \mu_{\delta}$ (mas/yr)	Sp.T.	Parallax (mas)
⁽¹⁾ WISEA J000430.66–260402.3	⁽¹²⁾ 1.127859, –26.067652	⁽¹²⁾ 57234.57	⁽¹²⁾ +1 ± 4, –244 ± 4	sdT2.0, ⁽¹²⁾ T4.0	⁽¹²⁾ 33.1 ± 4.7
⁽¹⁾ WISEA J030119.39–231921.1	⁽¹²⁾ 45.331221, –23.322665	⁽¹²⁾ 57262.58	⁽¹²⁾ +234 ± 3, –119 ± 4	sdT1.0	⁽¹²⁾ 37.3 ± 3.8
⁽¹⁾ WISEA J042236.95–044203.5	65.656712, –4.702669	58467.54	+1150 ± 53, –695 ± 55	T8.0 ± 1.0	
⁽²⁾ WISEA J155349.96+693355.2	238.445876, +69.567907	58358.98	–1684 ± 56, +1348 ± 53	⁽²⁾ T5.0 ± 1.0, ⁽³⁾ sdT4.0	
⁽³⁾ CWISE J221706.28–145437.6	⁽¹³⁾ 334.278402, –14.912140	⁽¹³⁾ 59826.03	⁽¹³⁾ +1257 ± 44, –986 ± 44	esdT5.5 ± 1.2	

For photometry:

Full name	α, δ (deg)	MJD	$\mu_{\alpha \cos \delta}, \mu_{\delta}$ (mas/yr)	Sp.T.	Parallax (mas)	Notes
⁽⁴⁾ CWISEP J015613.24+325526.6	29.0568626, +32.9235107	58419.89	+1138 ± 84, –373 ± 84	sdT		
⁽⁵⁾ CWISE J021948.68+351845.3	⁽¹⁴⁾ 34.9528878, +35.3125796	⁽¹⁴⁾ 57095.63	+673.2 ± 46.4, –504.4 ± 57.0	T9.5 ± 1.5	⁽¹⁵⁾ 57.33 ± 0.04	Ross 19B
⁽⁴⁾ CWISE J050521.29–591311.7	76.3403687, –59.2215888	58448.04	+461 ± 36, –1003 ± 35	T6.5		
⁽⁶⁾ CWISE J052306.42–015355.4	⁽¹⁴⁾ 80.7767575, –1.8987457	⁽¹⁴⁾ 57392.63	⁽¹⁴⁾ +511.6 ± 53.6, –39.9 ± 55.9	esdT0.0 ± 1.0		
⁽⁷⁾ WISEA J071121.36–573634.2	⁽¹⁴⁾ 107.8390823, –57.6092955	⁽¹⁴⁾ 56557.08	+18 ± 10, +990 ± 90	sdT0 ± 1		
⁽³⁾ CWISE J073844.52–664334.6	⁽¹⁴⁾ 114.6855096, –66.7262825	⁽¹⁴⁾ 57258.48	⁽¹⁴⁾ +768.4 ± 32.0, –445.1 ± 29.8	esdT5.5 ± 1.2		
⁽⁴⁾ CWISEP J090536.35+740009.1	136.4033148, +74.0008111	58494.02	+465 ± 67, –1490 ± 71	T6.0		
⁽¹⁾ WISEA J101944.62–391151.6	⁽¹⁴⁾ 154.9352802, –39.1974770	⁽¹⁴⁾ 57156.08	–472.2 ± 28.0, +222.7 ± 26.4	sdT3.0		
⁽⁸⁾ WISEA J153429.75–104303.3	233.621873, –10.721775	57645.36	–1253.1 ± 8.9, –2377.0 ± 7.0	esdY?	38.5 ± 8.4	The Accident
⁽⁹⁾ WISEA J200520.35+542433.6	⁽¹⁶⁾ 301.333016, +54.408501	⁽¹⁶⁾ 56658.00	⁽¹⁶⁾ –1154.4 ± 1.2, –900.4 ± 1.2	T8	⁽¹⁷⁾ 59.91 ± 0.55	Wolf 1130C
^(10,19) WISE J201404.13+042408.5	⁽¹⁸⁾ 303.516175, +4.402821	⁽¹⁸⁾ 57326.30	⁽¹⁸⁾ –611.3 ± 1.5, +313.4 ± 1.5	⁽¹⁹⁾ T6.5	⁽¹²⁾ 45.5 ± 2.4	
⁽¹⁾ WISE J210529.08–623558.7	⁽¹⁴⁾ 316.3716241, –62.5999392	⁽¹⁴⁾ 55961.60	⁽¹⁴⁾ 765.0 ± 15.7, –1507.2 ± 15.0	T1.5		
⁽²⁾ WISEAR J220746.67–503631.7	331.9449276, –50.6122455	58503.19	+108 ± 99, –1380 ± 98	T7.5		

References. (1): Greco et al. (2019); (2): Meisner et al. (2020b); (3): Meisner et al. (2021); (4): Meisner et al. (2020a); (5): Schneider et al. (2021) (6): Brooks et al. (2022); (7): Kellogg et al. (2018) (8): Kirkpatrick et al. (2021b); (9): Mace et al. (2013b); (10): Kirkpatrick et al. (2012) (11): Luhman & Sheppard (2014) (12): Best et al. (2020); (13): Zhang et al. (2023); (14): CatWISE, Marocco et al. (2021); (15): Parallax of the primary Ross 19A (Schneider et al. 2021); (16): Kirkpatrick et al. (2019); (17): Parallax of the primary Wolf 1130A (Mace et al. 2018); (18): Kirkpatrick et al. (2021a); (19): Mace et al. (2013a).

In this paper, we present the results from two-year ground-based parallax measurements of five metal-poor T dwarf candidates. We expand our previous work (Zhang et al. 2023) by obtaining z -band photometry of an extra 12 metal-poor T dwarf candidates, increasing the size of the metal-poor T dwarf sample from 12 to 24. We also present photometric constraints in five optical bands on the Accident. Section 2 describes the sample selection, the observation logs, and data reduction procedures. Section 3 analyses and discusses the data. Section 4 provides a summary and gives a prospective of the impact of this research.

2. Observations and data reduction

2.1. Astrometry

2.1.1. Sample

We selected six metal-poor T dwarf candidates to measure their trigonometric parallax: WISE0004 and WISE0301 (Greco et al. 2019), WISE0422 and WISE1553 (Meisner et al. 2020b), WISE2217 (Meisner et al. 2021), and WISEA J181006.18–101000.5 (Schneider et al. 2020). They all have z -band photometry from our previous work (Zhang et al. 2023). WISE1810 was measured to be the closest metal-poor brown dwarf with a distance to our Solar system of $8.9_{-0.6}^{+0.7}$ pc (Lodieu et al. 2022). In this chapter we focus on the remaining five objects, with their details listed in the upper part of Table 1.

2.1.2. Astrometric observation details

We used Omega2000 (Bailer-Jones et al. 2000; Baumeister et al. 2003; Kovács et al. 2004) on the 3.5-m telescope at the Calar

Alto Observatory, Andalucía, Spain. Omega2000 is an imager in the near-infrared (NIR) range equipped with a single 2048×2048 HAWAII-2 HgCdTe detector, covering a field of view (FoV) of 15'5 × 15'4. Its optics has very low dispersion, which allows accurate astrometry.

We carried out a two-year observing campaign from 2021 to 2022 to obtain enough astrometric epochs. We observed in the J band, under a monthly cadence, with a maximum seeing of 1''2, a maximum airmass of 1.8, and no constraint on the moon phase (programme numbers H20-3.5-020, F21-3.5-010, 22A-3.5-010, 22B-3.5-010; PI N. Lodieu). We set 9 to 10-point dithering pattern (and repeated it as necessary) for sky subtraction in the NIR, with different single exposure times for each observing block (OB) depending on the brightness of the object. The total exposure times were adjusted several times according to the results obtained in the previous semester. The details of the observations are presented in Table 2.

2.1.3. Astrometric data reduction

We reduced the J -band images using the Image Reduction and Analysis Facility (IRAF; Tody 1986, 1993). We bias and flat-corrected all the individual exposures using the master bias and master sky flat frames of the same night. We created the sky frame for each dithering point by median combining all the images of the other dithering positions in the same dithering cycle using the task *imcombine*, with scale parameter set to 'mode'. We subtracted the sky from each image using the task *imarith*. All the sky-subtracted images of the same epoch were then averaged via *imcombine*, taking into account the offsets. The pixels with the highest and the lowest deviating counts were rejected.

Table 2: Logs of the Omega2000 observations of five metal-poor T dwarf candidates. The data with notes 'bad' or 'no detection' are not used to solve the astrometry. The MJD indicates modified Julian date at the middle of the observation, MJD = JD - 2500000.5.

Name	MJD	Fil.	Exp.	Notes
W0004	59396.16	<i>J</i>	30s×18	
	59423.15	<i>J</i>	30s×18	
	59478.01	<i>J</i>	30s×9	
	59506.89	<i>J</i>	30s×9	
	59774.15	<i>J</i>	30s×9	
	59802.10	<i>J</i>	30s×9	
	59829.01	<i>J</i>	30s×9	
W0301	59856.89	<i>J</i>	30s×9	
	59242.78	<i>J</i>	30s×9	
	59269.78	<i>J</i>	30s×9	
	59423.16	<i>J</i>	30s×18	
	59478.15	<i>J</i>	30s×9	
	59507.07	<i>J</i>	30s×9	
	59598.77	<i>J</i>	30s×9	
W0422	59626.78	<i>J</i>	30s×9	
	59802.17	<i>J</i>	30s×9	
	59830.09	<i>J</i>	30s×9	
	59242.78	<i>J</i>	150s×10	bad
	59269.79	<i>J</i>	150s×10	
	59297.82	<i>J</i>	150s×10	
	59480.16	<i>J</i>	150s×20	
W1553	59507.09	<i>J</i>	150s×20	
	59598.79	<i>J</i>	150s×20	
	59626.81	<i>J</i>	150s×20	bad
	59830.16	<i>J</i>	150s×20	
	59242.78	<i>J</i>	150s×10	
	59297.82	<i>J</i>	150s×10	
	59325.14	<i>J</i>	150s×10	bad
W2217	59395.96	<i>J</i>	50s×100	
	59506.83	<i>J</i>	150s×20	
	59571.22	<i>J</i>	150s×20	
	59598.22	<i>J</i>	150s×20	
	59627.19	<i>J</i>	150s×20	
	59716.08	<i>J</i>	150s×20	
	59746.06	<i>J</i>	150s×20	
	59772.85	<i>J</i>	150s×20	
	59801.87	<i>J</i>	150s×20	
	59828.86	<i>J</i>	150s×20	
	59856.82	<i>J</i>	150s×20	
W2217	59396.12	<i>K_s</i>	30s×60	no det.
	59423.01	<i>J</i>	150s×20	bad
	59477.97	<i>J</i>	150s×20	
	59480.04	<i>J</i>	150s×20	
	59506.85	<i>J</i>	150s×20	
	59716.14	<i>J</i>	150s×20	
	59746.12	<i>J</i>	150s×20	
	59774.11	<i>J</i>	150s×20	
	59802.06	<i>J</i>	150s×20	bad
	59828.90	<i>J</i>	150s×20	bad
59856.85	<i>J</i>	150s×20		

We used the task *daofind* with a threshold of 10σ , an average full width half maximum (FWHM) of point source, and an average background fluctuation of each image to extract the point sources with high signal-to-noise-ratio (S/N). These high-S/N point sources are key to determine the shift, rotation, magnifica-

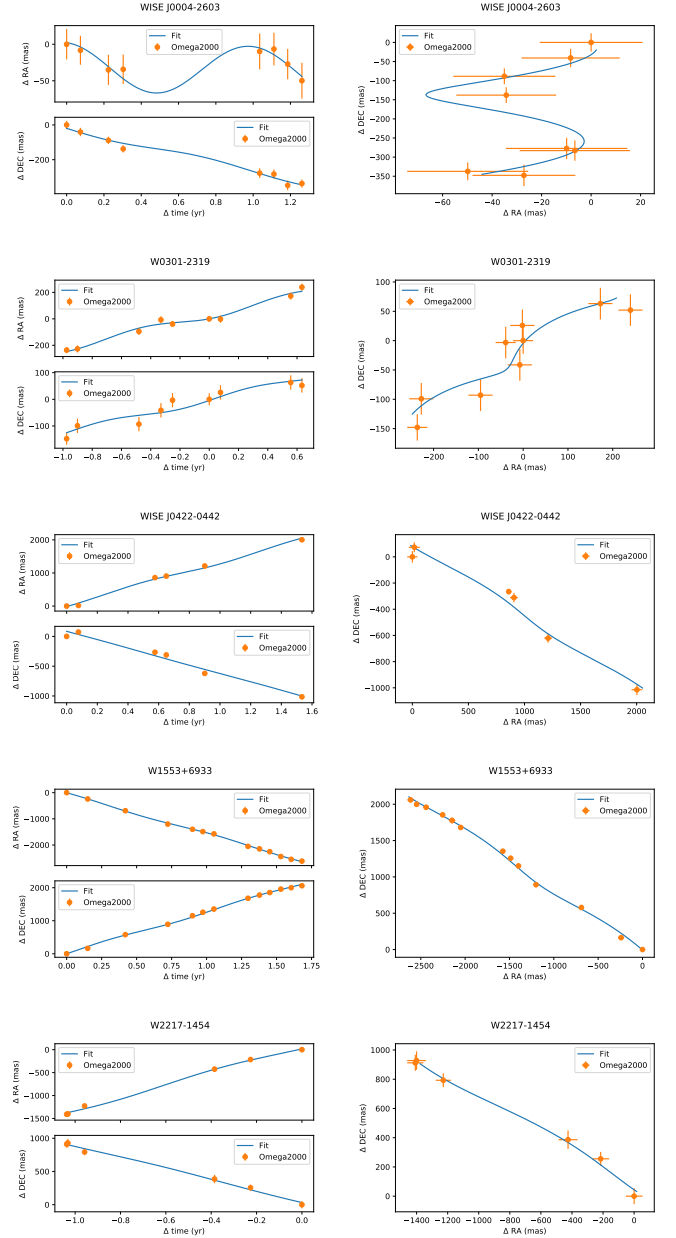


Fig. 1: Astrometry for five metal-poor T dwarf candidates. *Left*: observed relative astrometry separated in RA and Dec against the relative time of the reference epoch (0.0 year). *Right*: observed relative astrometry together in RA and Dec.

tion of the field, as well as the optical aberrations. Our targets, on the other hand, are normally faint, so we used *imcentroid* to locate the target if it was not extracted with the 10σ threshold. We then used the task *xyxymatch* to match all the extracted sources between the reference epoch and each other epoch. In the next step, we used *geomap* and *geoxytran* to fit the pixel-level transformation between epochs and transform the target pixel coordinates of the different epochs to the reference frame of the reference epoch (0.0 year in Fig. 1). At the end, we obtained the absolute differences of the target coordinates in pixels between epochs. The errors in both axes are the quadratic sums of the centroid error and the residuals from the fitting of the task *geomap*. The pixel scale of Omega2000 obtained for the images of

Table 3: Our astrometry solutions of five metal-poor T dwarf candidates.

Name	$\mu_{\alpha \cos \delta}$ (mas/yr)	μ_{δ} (mas/yr)	ϖ (mas)
W0004	-5.5 ± 12.2	-248.0 ± 9.7	32.3 ± 9.8
W0301	252.9 ± 16.7	125.5 ± 16.6	26.4 ± 9.8
W0422	$+1286.4 \pm 35.2$	-708.2 ± 50.4	46.6 ± 24.2
W1553	-1526.7 ± 12.4	$+1258.4 \pm 12.7$	38.5 ± 8.4
W2217	$+1352.4 \pm 22.8$	-843.8 ± 23.5	48.0 ± 13.2

W1810 (449.45 ± 0.45 mas/pix; Lodieu et al. 2022) was used for all the five sources studied in this paper.

The difference of the coordinates in RA α and Dec δ should follow

$$\Delta\alpha \cdot \cos \delta = \mu_{\alpha \cos \delta} (t_i - t_0) + \varpi (f_i^{\alpha} - f_0^{\alpha}) + k_{\alpha};$$

$$\Delta\delta = \mu_{\delta} (t_i - t_0) + \varpi (f_i^{\delta} - f_0^{\delta}) + k_{\delta},$$

where t is the time in year, 0 and i stand for the reference epoch and the i -th epoch, μ is the proper motion in mas/yr, ϖ is the parallax in mas, f^{α} and f^{δ} are the parallax factors for the right ascension and declination. The parallax factors were computed using the Earth geocenter as obtained from the JPL DE441 solar system ephemeris (Park et al. 2021). k is a small offset in both axes that allows better statistical solutions. We solve the astrometry by applying a minimisation method. We visualise the fitting in Fig. 1 and the results are given in Table 3. We report three completely new parallaxes for metal-poor T dwarf candidates: W0422, W1553, and W2217. Our results for the two brightest objects, W0004 and W0301, are consistent at the $1-\sigma$ level with the values obtained by Best et al. (2020) shown in Table 1. For these two objects, we will use our parallax determinations for this research.

2.2. Optical photometry

2.2.1. Sample

Our sample for far-red optical photometry consists of 12 metal-poor T dwarf candidates from the literature, complementing the 12 metal-poor T dwarf candidates in our previous work (Zhang et al. 2023):

- W0156, W0505, and W0905 were identified because of their red $J - ch2$ and blue $ch1 - ch2$ Spitzer colours (Meisner et al. 2020a). A red $J - ch2$ colour suggests low temperature (Meisner et al. 2023c). W0505 has a large reduced proper motion and a high tangential velocity (Meisner et al. 2023c). W0905 also has a high proper motion (Meisner et al. 2020a).
- The late-type T9.5 subdwarf W0219 (Ross 19B) was discovered by the Backyard Worlds: Planet 9 citizen science project (Kuchner et al. 2017) to be a comoving companion to Ross 19A. The primary is an M3.5 subdwarf with a metallicity of $[Fe/H] = -0.40 \pm 0.12$ dex (Schneider et al. 2021). However, the secondary lacks spectroscopy.
- W0523 was discovered by Goodman (2021); Brooks et al. (2022) and was classified it as an extreme T subdwarf candidate based on its distinctive infrared colours and high proper motion. Its locus in the $W1 - W2$ versus $J - W2$ colour-colour diagram is similar to those of extreme T subdwarf candidates W1810 and WISEA J041451.67–585456.7 (Schneider et al. 2020).

- W0711 was discovered by the AllWISE2 Motion Survey as a possible thick-disk early-T subdwarf, with a tentative low metallicity (Kellogg et al. 2018).
- W0738 was discovered by Meisner et al. (2021), based on its large motion and also colours similar to those of the two extreme T subdwarf W1810 and W0414 (Schneider et al. 2020).
- W1019 was identified as an early T subdwarf together with W0004 and W0301, by Greco et al. (2019) based on their blueish NIR spectrum.
- The benchmark late-type T8 subdwarf W2005 (Wolf 1130C) belongs to the triple system Wolf 1130. Wolf 1130A is a M subdwarf and Wolf 1130B is an ultramassive white dwarf, tidally locked with Wolf 1130A. This system is old (> 3.7 Gyr) and metal-poor, with a subsolar iron abundance derived from the M subdwarf Wolf 1130A, although with a discrepancy from -0.62 ± 0.10 to -1.22 ± 0.24 dex (Woolf & Wallerstein 2006; Mace et al. 2013b; Newton et al. 2014; Mace et al. 2018).
- W2014 was discovered by Mace et al. (2013a) in WISE and it has a suppressed K-band spectrum. Its IR colour just falls outside the extreme T subdwarf IR colour-colour criteria (Meisner et al. 2023c).
- W2105 was discovered as a thick-disk or halo early T dwarf, although its YJH -band spectrum does not show an obvious signature of low metallicity (Luhman & Sheppard 2014). Meisner et al. (2023c) shows that it lies outside but next to the extreme T subdwarf IR colour-colour criteria. It is worthwhile to have the optical photometry done to see its optical-IR colour behaviour.
- W2207 was identified by Meisner et al. (2020b) as potential subdwarf owing to its high kinematics, and red $J - ch2$ colour.

We also include the enigmatic brown dwarf WISEA J153429.75–104303.3 (a.k.a. "The Accident", Meisner et al. 2020b; Kirkpatrick et al. 2021b). Thanks to its extremely high proper motion, it was recently found by citizen scientist Dan Caselden in the Near-Earth Object Wide-field Infrared Survey Explorer Reactivation Mission (NEOWISE; Mainzer et al. 2014) data. It possesses peculiar NIR colours compared to normal Y dwarfs discovered so far. With robust parallax measurements (distance $16.3_{-1.2}^{+1.4}$ pc), its absolute J , $W2$, and $ch2$ magnitudes are in line with the coldest known Y dwarfs but the $W1$ and $ch1$ bands are abnormally bright (Kirkpatrick et al. 2021b). It is suspected to be the first and the only metal-poor Y dwarf to date: it is cold, with an effective temperature of $T_{\text{eff}} = 400 - 550$ K, while the T/Y transition temperature is $T_{\text{eff}} \approx 485$ K for solar-metallicity dwarfs (Leggett et al. 2021); and is low in metallicity, likely to be lower than -1.0 dex (Kirkpatrick et al. 2021b; Meisner et al. 2023c). All metal-poor T and Y dwarf candidates with optical photometry are also listed in Table 1.

2.2.2. Photometric observation details

We downloaded co-added z -band images of W0505, W2105, and W2207 from the Dark Energy Survey (DES; Abbott et al. 2021) archive. However, there are no detection for W0505 or W2207. We requested deeper imaging of these two objects, described in the following paragraphs. For W2105, the motion is clearly seen in the different epochs. We adopted the DR1 z_{DES} magnitude (Abbott et al. 2018), since in the DR2 catalogue W2105 was recognised as three different objects in the multi-epoch co-added images.

We collected z -band images of three metal-poor T dwarf candidates in the northern hemisphere: W0523, W0905 and

Table 4: Logs of new optical observations of the Accident and the other 11 metal-poor T dwarf candidates. The MJD indicates the time in modified Julian date format at the middle of the observation. MJD = JD – 2500000.5.

Name	MJD	Seeing	Moon	Instrument	Filters	On-source integration time
The Accident	60466.07	0".8	Dark	GTC/HiPERCAM	$u'g'r'i'z'$	60.5s×124=7502s
The Accident	60473.98	0".8	Grey-Dark	GTC/HiPERCAM	$u'g'r'i'z'$	60.9s×180=10962s
W0156	60565.35	0".6	Dark	VLT/FORS2	z_{Gunn}	120s×24=2880s
Ross 19B	60565.30	0".5	Dark	VLT/FORS2	z_{Gunn}	120s×24=2880s
W0505	60578.21	0".7	Grey	VLT/FORS2	z_{Gunn}	120s×20=2400s
W0523	60227.20	0".8	Grey	GTC/OSIRIS+	z'	60s×48=2880s
W0711	60565.38	0".6	Dark	VLT/FORS2	z_{Gunn}	60s×8=480s
W0738	60407.13	0".6	Dark	VLT/FORS2	z_{Gunn}	120s×16=1920s
W0905	60606.19	1".0	Bright	GTC/OSIRIS+	z'	60s×48=2880s
W1019	60468.06	0".7	Dark	VLT/FORS2	z_{Gunn}	60s×8=480s
Wolf 1130C	60210.97	0".8	Grey	GTC/OSIRIS+	z'	60s×48=2880s
W2014	60562.22	0".9	Dark	VLT/FORS2	z_{Gunn}	120s×16=1920s
W2207	60622.16	0".7	Dark	VLT/FORS2	z_{Gunn}	120s×24=2880s

Wolf 1130C with the upgraded Optical System for Imaging and low-Intermediate-Resolution Integrated Spectroscopy (OSIRIS+) on the GTC (programmes GTC13-23B & GTC31-24B; PI J.-Y. Zhang). OSIRIS+ is an imager and spectrograph for the optical wavelength range, an upgraded version of OSIRIS (Cepa et al. 2000), located in the Cassegrain focus of GTC. It is equipped with a 4096×4096 deep-depleted e2v CCD231-842 (astro-2 coating) detector, with an unvignetted field of view of 7.8×7.8 and a 2×2 -binned pixel scale of $0''.254/\text{pix}$.

We also collected z -band images of eight objects: W0156, Ross 19B, W0505, W0711, W0738, W1019, W2014 and W2207 using the FOcal Reducer/low dispersion Spectrograph 2 (FORS2; Appenzeller et al. 1998) mounted on the Cassegrain focus of the 8.2-m Antu Unit Telescope (UT1) of the European Southern Observatory (ESO) Very Large Telescope (VLT) at Cerro Paranal, Chile, through ESO programme 113.2688 (PI J.-Y. Zhang). FORS2 is an optical imager, polarimeter and spectrograph. It is equipped with a mosaic of two 2048×4096 MIT/LL CCID-20, backside illuminated, AR coated CCDs: chip 1 and chip 2. We used the high resolution collimator which produces an FoV of 4.25×4.25 and a pixel scale of $0''.125/\text{pix}$ with the standard 2×2 binned readout modes. We always put the target on the chip 1 of FORS2. We used the z_{Gunn} filter, which is similar to the Sloan z' filter.

We requested a four-point dithering pattern (only one cycle) with several contiguous exposures at each point. For the GTC we set the single exposure time to 60s and for the VLT we set it to 120s to avoid saturation because of the sky background. Except for W0711 and W1019, we set an single exposure time of 60s on the VLT and without dithering to save the overheads, since they are clearly detected in a single exposure.

We collected photometry of the Accident simultaneously in the $u'g'r'i'z'$ bands using the High PERformance CAMera (HiPERCAM; Dhillon et al. 2021) on the 10.4-m Gran Telescopio Canarias (GTC) at Roque de los Muchachos Observatory on the island of La Palma, Spain, programme GTC51-24A (PI J.-Y. Zhang). HiPERCAM is a quintuple-beam, high-speed optical imager equipped with four dichroic beamsplitters and five custom-made Teledyne e2v CCD231-42 detectors. Each detector has an FoV of 2.8×1.4 , or 3.1 in diagonal and a pixel scale of $0''.081/\text{pix}$ without binning. We requested in total five OBs under service mode of GTC. The total on-source exposure time is 5.1h. We set a four-point dithering pattern with 15 exposures of 60s at each point for each OB, with a 2×2 binning. The dithering was set specially for the sky subtraction in the z band while saving

as much overheads as possible. Our weather constraints were set to be seeing better than $0''.9$, dark nights, and clear sky. The first two OBs were executed on the first-half of the night on June 4, 2024 and three more OBs were executed on the first-half of the night on June 11, 2024. All the photometric observations details are listed in Table 4.

2.2.3. Photometric data reduction

The individual HiPERCAM exposures were bias and flat-field corrected by the HiPERCAM pipeline. For each band, we created a supersky frame by median combining a third of all the frames (around 100 frames) with lowest counts and without the position offsets using the *imcombine* task of IRAF. The zero offset was set to be the mode value of all the counts. The supersky was subtracted from each frame using the task *imarith*. We stacked all the sky subtracted frames and rejected the two highest- and two lowest pixels using *imcombine*, with the zero offset set to be the mode value. The dithering position offsets were manually measured through the *imexam* task.

The individual OSIRIS+ images were bias and flat-field corrected manually using IRAF. The individual FORS2 exposures were bias and flat-field corrected by the FORS pipeline run in the EsoReflex environment (Freudling et al. 2013). First, the sky frame of each position in the four-point dithering pattern was created by mode-scaling and median-combining all the images at the other three positions, but two-thirds of the highest counts were rejected. The corresponding sky frame was then subtracted from all the images. Finally, all the sky-subtracted images were aligned and average-combined, but the two highest and two lowest pixels were rejected.

2.2.4. Object recognition

We created the world coordinate system (WCS) for all reduced images using *Astrometry.net* (Lang et al. 2010), which extracts stars and solves the WCS by matching subsets of four stars to the pre-computed 4200 series index with the 2MASS catalogue as reference. For W2207, because there are not many bright 2MASS stars in the field, we built our own index file based on the Dark Energy Survey (DES; Abbott et al. 2021) catalogue. We projected the expected positions of the objects in the images based on their proper motions. Table 1 lists the proper motions from the literature. We drew a circle with a radius equal to the

error centred on the expected position for each target, as shown in Fig. A.1.

Table 5: Revised astrometry of W0156 and W0711 with the astrometry rms, the centroid errors, and the pixel sizes.

W0156 at MJD 60565.35	
α, δ (deg)	29.058675, 32.923258
rms _{X,Y} (pix)	1.274, 0.920
err _{X,Y} (pix)	0.239, 0.224
scale (mas/pix)	127.67
$\mu_\alpha \cos \delta, \mu_\delta$ (mas/yr)	+1020 ± 29, -155 ± 22
W0711 at MJD 60565.38	
α, δ (deg)	107.840390, -57.606015
rms _{X,Y} (pix)	0.589, 0.725
err _{X,Y} (pix)	0.030, 0.029
scale (mas/pix)	125.53
$\mu_\alpha \cos \delta, \mu_\delta$ (mas/yr)	+230 ± 9, +1076 ± 11

We detected all the objects at their expected positions, except for W0156, W0711, and the Accident. We recognised W0711 using the DESI Legacy Survey DR10 image, and we attribute the faint source next to the expected position of W0156 as its true position. We indicated W0156 and W0711 using red arrows in Fig. A.1. We revised their proper motions following the same routine as we did in Zhang et al. (2023). The IRAF *imcentroid* task was used to provide the centroid error in both axes. The astrometry residuals of both axes are the standard error of the mean (SEM) of the pixel deviation between the index position and field position of the matched reference stars (match_weight > 0.99) in the corr.fits file generated by *Astrometry.net*. The revised proper motion results are shown in Table 5.

2.2.5. Photometric measurement

We performed aperture photometry on these 11 detected metal-poor T dwarf candidates using the *Astropy* package *photutils*. The aperture radius was fixed to be 1'', and the background residual after the sky subtraction is from the median absolute deviation within an annulus with an inner and outer radius of 3''.5 and 5''.5, respectively. W0523, W1019 and W2014 were close to other background sources, hence, we set a smaller aperture with a radius of 0''.5 for these three objects only. For these three, we did a consistency check using a programme *daofun*¹ (Quezada et al. in prep.) which is an interactive adaption of *daophot* (Stetson 1987) to easily go through the *daophot* subroutines to perform a point-spread-function (PSF) photometry. Using the GUI we automatically picked brighter and isolated stars over the background noise and check by eye with the GUI each point spread function to then create the PSF model. The PSF photometry is based on the ALLSTAR subroutine of *daophot* also included in the *daofun* GUI, we activate the variable PSF parameter, set the FWHM of stars by 4 pixels, the fitting radius by 6 pixels and the PSF radius by 12 pixels as the GUI recommended parameters.

For these 11 detected metal-poor T dwarf candidates, we did differential photometry using an extra set of several nearby sources from The Panoramic Survey Telescope and Rapid Response System (Pan-STARRS; Chambers et al. 2016), SkyMapper Southern Sky Survey (Onken et al. 2024), and the DES with z magnitudes fainter than 16 mag in the AB system).

Since there are no detection of the Accident in any of the HiPERCAM bands, we estimated a 3- σ detection limit by con-

servatively assuming a 3- σ signal would have a total flux inside the 1.5-FWHM-radius (1''/2) aperture of $3 \times \sigma_{sky} \times \sqrt{N_{pix}}$ where σ_{sky} is the fluctuation or standard deviation inside the aperture, and N_{pix} is the pixel number inside the aperture. For the $g'r'i'z'$ bands we did differential photometry using an extra set of several nearby Pan-STARRS sources with magnitudes fainter than 16 mag. The 3- σ limits set in this way in the $g'r'i'z'$ bands are very well consistent with the aperture photometry on the faintest sources (S/N less than 10 σ) in the field. For the u' band of HiPERCAM we calculated the limit using the zero point value of 28.17 mag provided by the GTC², since there is no u' -band survey in this region.

For the T and Y dwarfs, a correction for each spectral type must be applied to convert Sloan z' magnitudes, or DES z_{DES} magnitudes to Pan-STARRS z_{PS1} magnitudes, due to significant difference between filter profiles longwards of 9300Å. Following the procedure of Zhang et al. (2023), we applied the offsets calculated from T dwarf standards and Y dwarf models. Table 6 lists the $u'g'r'i'z'$ and z_{DES} photometry directly determined from the observations and the z_{PS1} after the correction. Other IR photometric measurements from the literature are also listed in that table.

3. Discussion

3.1. Colour–magnitude diagrams

With trigonometric parallaxes, we could derive the absolute magnitudes of subdwarfs and position them in colour-magnitude diagrams. For the distance of two companions, i.e., Wolf 1130C and Ross 19B, we used well-determined parallaxes from their primaries, Wolf 1130A and Ross 19A, respectively. Both objects have well-constrained spectroscopic metallicities derived from their primary. Hence, they are benchmarks in our sample.

We plotted several colours of nine metal-poor T dwarf candidates and the Accident against their absolute z_{PS1} magnitudes in Fig. 2. In this figure, we overplotted solar-metallicity field M, L, T dwarfs with trigonometric parallaxes from Pan-STARRS1 (Best et al. 2018) as well as several colder objects with z' -band magnitudes from GTC/OSIRIS (Lodieu et al. 2013; Martín et al. 2024) and trigonometry parallaxes (Kirkpatrick et al. 2019), along with four Y0 dwarfs published by Cushing et al. (2011) WISE J014656.66+423410.0, WISE J041022.71+150248.4, WISEP J173835.52+273258.9, and WISE J205628.91+145953.2; and a Y2 dwarf also from Cushing et al. (2011) WISE J182831.08+265037.7. We also included a cold binary system, WISE J121756.90+162640.8, which consists of a T9 dwarf and a Y0 dwarf (Liu et al. 2012), supposed to be overluminous compared to single T9 and Y0 dwarfs. We use motion-corrected photometry from CatWISE catalogue (Marocco et al. 2021) for all Y dwarfs.

From Fig. 2, we could infer the following points:

- The benchmark Wolf 1130C is most probably a T subdwarf. It is located below the faintest T dwarf in the solar-metallicity sequence, confirming its low metallicity (from -0.6 to -1.2 dex) and its late spectral type.
- W1553, W1810 and W2217 are also most probably T subdwarfs. Again, W2217 lies below the faintest T dwarf in the solar-metallicity sequence, suggesting it could be the coldest or most metal-poor object among the three.

² <https://www.gtc.iac.es/instruments/hipercam/hipercam.php>

¹ <https://pypi.org/project/daofun/0.2.0/>

Table 6: New optical photometry and published IR photometry of the Accident, and other 12 metal-poor T dwarf candidates. If not specified otherwise, the reference for the IR photometry will be the same as the one for the object in Table 1. The optical photometry are under the AB system (Oke 1974). The *JHK* photometry are under the MKO system unless specified.

Name	u'	g'	r'	i'	z'	z_{DES}	z_{PS1}	Y	J	H	K	W1	W2
The Accident	>28.7	>27.9	>27.6	>27.3	>26.2		>26.7	⁽¹⁾ >21.79	⁽²⁾ 24.5 ± 0.3	>18.58	$K_s > 17.85$	18.18 ± 0.19	16.15 ± 0.08
W0156					24.70 ± 0.24		25.42 ± 0.31	⁽²⁾ 21.94 ± 0.06	21.46 ± 0.30			18.81 ± 0.42	16.06 ± 0.08
Ross 19B					25.10 ± 0.33		25.80 ± 0.40	⁽²⁾ 21.86 ± 0.06	21.14 ± 0.02			18.62 ± 0.20	15.81 ± 0.06
W0505					25.24 ± 0.36	* >23.4	26.09 ± 0.36		⁽²⁾ 20.74 ± 0.07	⁽²⁾ 20.62 ± 0.08	$K_s > 18.38$	** 17.64 ± 0.06	** 16.13 ± 0.05
W0523					22.10 ± 0.03		22.74 ± 0.15		⁽²⁾ 19.14 ± 0.05			17.27 ± 0.06	15.91 ± 0.06
W0711					19.48 ± 0.03		20.09 ± 0.12					15.09 ± 0.03	14.63 ± 0.04
W0738					24.29 ± 0.19		25.23 ± 0.20		⁽²⁾ 21.37 ± 0.14	⁽²⁾ 20.73 ± 0.14	⁽²⁾ 21.44 ± 0.34	17.22 ± 0.04	15.82 ± 0.04
W0905					24.08 ± 0.09		24.97 ± 0.13		20.45 ± 0.14			18.25 ± 0.16	16.46 ± 0.09
W1019					19.27 ± 0.01		20.16 ± 0.08		⁽³⁾ 16.03 ± 0.10	⁽³⁾ 15.77 ± 0.13	⁽³⁾ K_s 15.73 ± 0.27	15.65 ± 0.04	14.22 ± 0.04
Wolf 1130C					22.64 ± 0.05		23.50 ± 0.19		19.64 ± 0.09	19.57 ± 0.07		^{(4),†} 17.16 ± 0.04	⁽⁴⁾ 15.14 ± 0.02
W2014					21.52 ± 0.03		22.36 ± 0.5		⁽⁵⁾ 18.01 ± 0.02	⁽⁵⁾ 18.71 ± 0.30	⁽⁵⁾ 17.97 ± 0.29	⁽⁴⁾ 16.66 ± 0.04	⁽⁴⁾ 14.83 ± 0.03
W2105						19.49 ± 0.01	20.19 ± 0.02	⁽²⁾ 17.96 ± 0.03	⁽³⁾ 16.85 ± 0.14	⁽²⁾ 15.91 ± 0.03	⁽³⁾ 15.31 ± 0.15	⁽²⁾ 14.82 ± 0.01	⁽²⁾ 13.93 ± 0.02
W2207					24.23 ± 0.10	* >23.4	25.20 ± 0.12		>20.36	>18.98	$K_s > 18.38$	⁽⁴⁾ 18.88 ± 0.27	⁽⁴⁾ 16.01 ± 0.07

References. (1): Meisner et al. (2023b) (2): Meisner et al. (2023c); (3): 2MASS point source catalogue (Cutri et al. 2003); (4): Profile-fit photometry including motion from CatWISE catalogue (w1mpro_pm and w2mpro_pm column) (Marocco et al. 2021); (5): Best et al. (2021)
Notes: *: Single-epoch DES 3- σ z -band limit under the AB system, as inferred from the 10- σ limit 22.1 mag (Morganson et al. 2018; Abbott et al. 2021); **: From the WISE and DES images we notice that the WISE photometry may be slightly contaminated by a background source. †: There are two CatWISE detections with similar proper motion values. We adopted the W1, W2 values of the one with more profile-fit flux measurements with S/R no less than 3 in both bands (column names w1NM and w2NM).

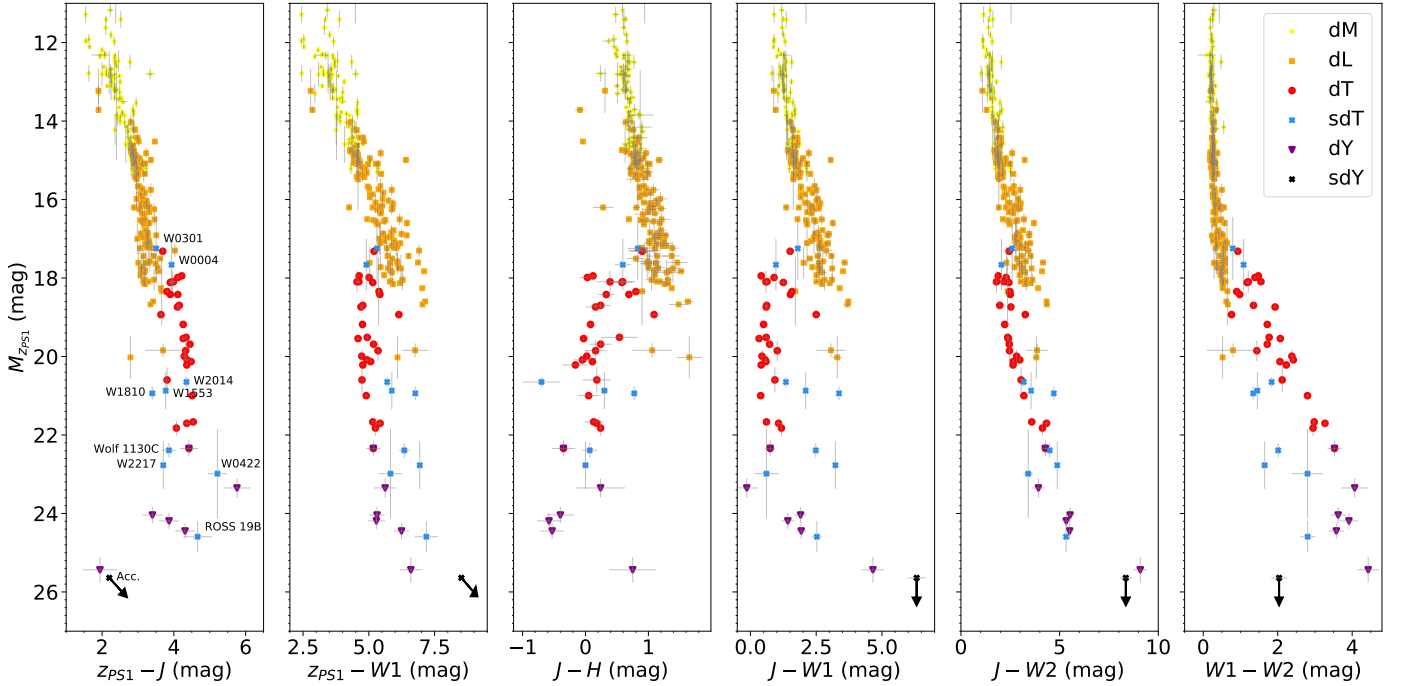


Fig. 2: Colours vs. absolute z_{PS1} magnitude diagrams of metal-poor T dwarf candidates (blue crosses), using trigonometric parallaxes obtained from this work and from the literature, z_{PS1} photometry from this work and from Zhang et al. (2023) and infrared photometry from the literature. The parallax of W1810 comes from Lodieu et al. (2022). For the Accident (black cross and arrow), the parallax is from (Kirkpatrick et al. 2021b). For comparison, field M, L, T dwarfs with trigonometric parallaxes from Pan-STARRS1 3 π survey (Best et al. 2018) are plotted as yellow stars, orange squares, and red dots, respectively. Y dwarfs with z_{PS1} photometry (corrected from z') from Lodieu et al. (2013) and Martín et al. (2024), and parallaxes from Kirkpatrick et al. (2019) are plotted as purple triangles. W1217 is a T9+Y2 system so it is plotted as a mixture of red dot and purple triangle.

- W0422's absolute magnitude is fainter than that of the faintest solar-metallicity T dwarf but only at a 1.5- σ significance. It suggests a possible colder nature of W0422, or a probable slightly low metallicity.
- Ross 19B lies way below the T dwarf sequence. It inherits the metallicity of -0.4 dex from its primary but without a spectroscopic confirmation of the secondary itself. Comparing with Wolf 1130C, which is also a late-type subdwarf and with a much lower metallicity, the difference between the absolute z_{PS1} magnitude of Ross 19B and those of the T dwarf sequence seems to be too large. This suggests, either Ross 19B is a colder object, or less likely that it has a lower metallicity than the value from its comoving primary.
- W0004 and W0301 lie on top of the sequence of early-T dwarfs in all the six colour-magnitude diagrams, which suggests that they are not so metal-poor, as corroborated by their optical spectra (Zhang et al. 2023) and slightly blue NIR

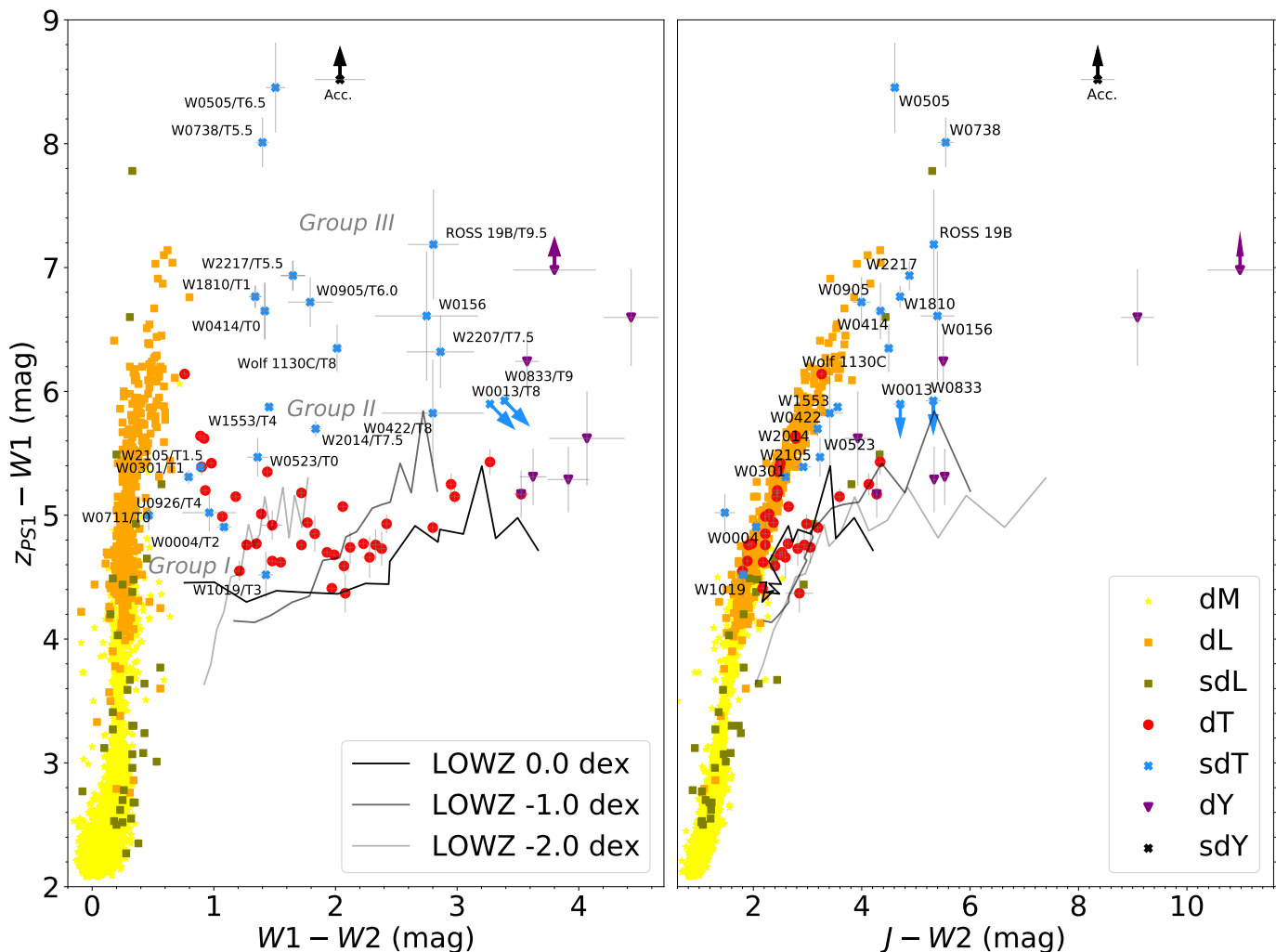


Fig. 3: Updated $W1 - W2$ vs $z_{AB} - W1$ and $J - W2$ vs $z_{AB} - W1$ colour-colour diagrams with more metal-poor T, Y dwarf candidates compared to the one of Zhang et al. (2023). All the metal-poor T dwarf candidates are labeled with blue crosses and arrows and the Accident is labeled with the black cross and arrow. We overplotted solar-metallicity M, L, and T sequences from Pan-STARRS (yellow stars, orange squares and red dots, respectively), L subdwarfs (olive squares), four Y0 dwarf, a Y2 dwarf, the Y4 dwarf (purple triangles), and a T9+Y0 system (red dot mixed with purple triangle). All Y dwarfs are with CatWISE photometry. Error bars are included for all sources, except for M and L dwarfs. We also show three iso-metallicity curves from the low-metallicity theoretical model LOWZ with parameters $\log g = 5.0$, $\log_{10} K_{zz} = 2$, solar C/O ratio 0.55 in both diagrams. From left to right, the effective temperature of the model decreases from 1600 K to 500 K, with a step of 100 K and 50K above and under 1000K, respectively.

spectra (Greco et al. 2019), or they could be equal-mass binaries.

- W2014 has a slightly red $z_{PS1} - J$, $z_{PS1} - W1$ colours and a slightly blue $W1 - W2$ colour, similar to those T subdwarfs. It lies on top of the sequence of solar-metallicity mid-T dwarfs in the diagram of $z_{PS1} - J$ and $J - W2$, which suggests that its metallicity is not extremely low. It has a bluer $J - H$ colour with a $2\text{-}\sigma$ significance.
- The Accident is below the faintest solar-metallicity Y dwarf in all diagrams, arguing in favour of its low-metallicity and cold nature.

In summary, we confirm the subluminosity of four T subdwarfs: Wolf 1130C, W1553, W1810, and W2217 and one Y subdwarf, the Accident. We also have another three possible subdwarfs: Ross 19B, W0422, and W2014 in these colour-magnitude diagrams. These objects seems to lie to the blue of the sequence

in the following colours: $z_{PS1} - J$ and $W1 - W2$; and to the red in the colours $z_{PS1} - W1$ and $J - W1$. $J - H$ and $J - W2$ colours do not seem to be good metallicity indicators because most of metal-poor objects lie on the solar-metallicity sequence. We are going to discuss more about the colours in the next subsection.

3.2. Colour-colour diagrams

Figures 3 and 4 update the colour-colour diagrams of $W1 - W2$ versus $z_{PS1} - W1$ and $J - W2$ versus $z_{PS1} - W1$ for all the objects, with 8508 solar-metallicity M dwarfs, 800 L dwarfs, and 42 T dwarfs from Pan-STARRS1 with and without trigonometric parallaxes (Best et al. 2018), four Y0 dwarfs W0146, W0410, W1738, W2056, a Y2 dwarf W1828, and the T9+Y0 binary W1217. We added the $z_{PS1} - W1$ limit of the Y4 dwarf WISEJ085510.83–071442.5 (Luhman 2014)

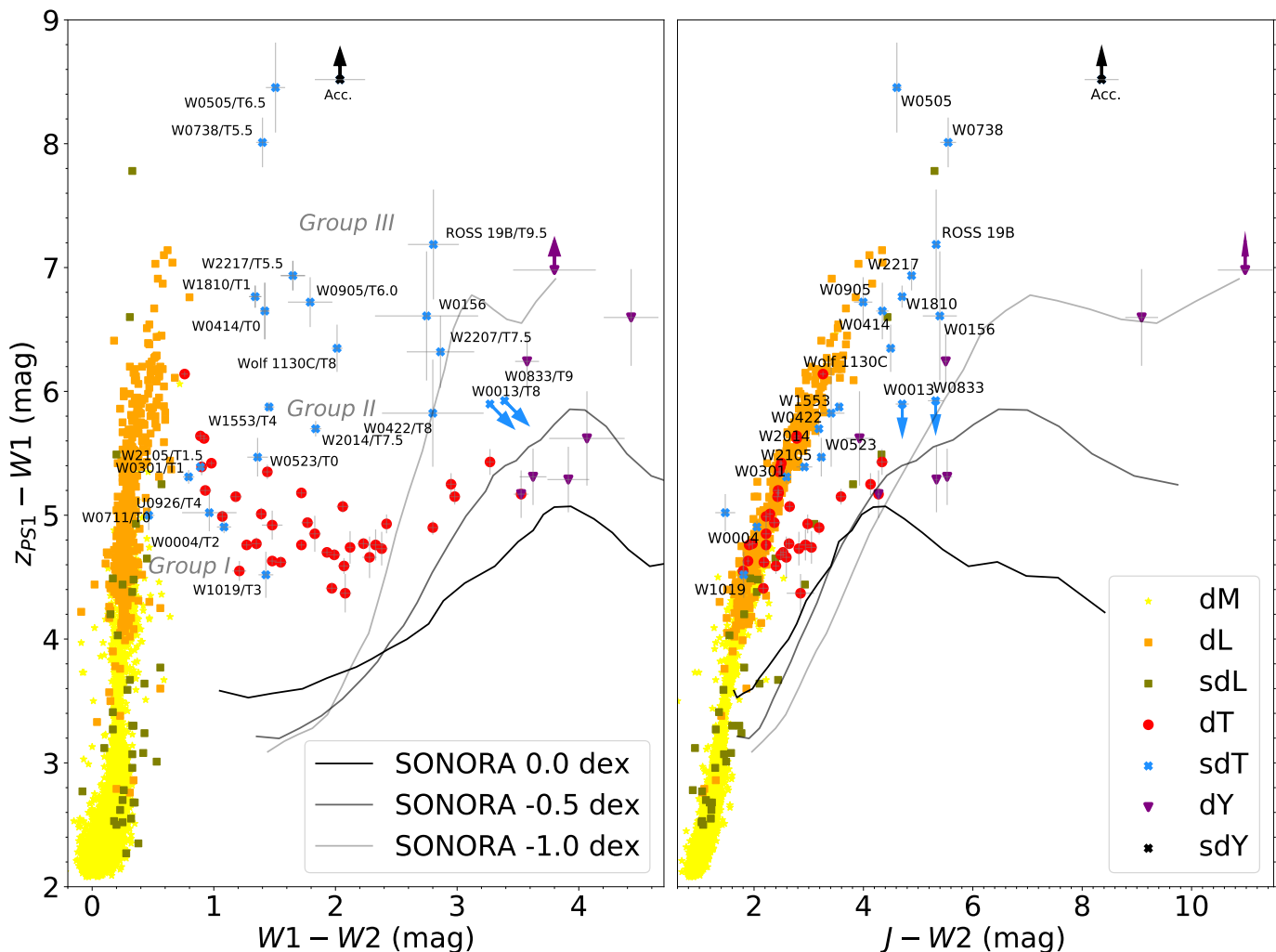


Fig. 4: The same as Fig. 3 but with three iso-metallicity curves from the theoretical model SONORA Elf Owl with parameters $\log g = 5.0$, $\log_{10} K_{zz} = 2$, solar C/O ratio in both diagrams. From left to right, the effective temperature of the model decreases from 1500 K to 300 K, with a step of 100 K, 50 K and 25 K at the temperature above 1000 K, between 600 K - 1000 K and below 600 K, respectively.

which is the coldest brown dwarf discovered so far (Beamín et al. 2014; Luhman et al. 2024). There are also 39 L subdwarfs with photometric errors smaller than 0.2 mag in z , J , $W1$, and $W2$ bands (Zhang et al. 2018). Three objects, WISEA J001354.40+063448.1, WISEA J083337.81+005213.8, and ULAS J092605.47+083516.9, included in our previous work are kept (Zhang et al. 2023).

We compared the observations with synthetic photometry derived using filter profiles downloaded from the Spanish Virtual Observatory (SVO) service (Rodrigo et al. 2012; Rodrigo & Solano 2020), and theoretical spectra from the low-metallicity ultracool LOWZ models (Meisner et al. 2021) and the SONORA Elf Owl substellar atmosphere models for T and Y dwarfs (Mukherjee et al. 2024; Mukherjee et al. 2023a,b). We used the following parameters: a high surface gravity $\log(g) = 5.0$, a medium vertical mixing $\log_{10} K_{zz} = 2$ and a solar C/O ratio of 0.55 for both the LOWZ and the SONORA model. The LOWZ models provide spectra down to metallicity -2.5 dex while the SONORA models only reach to -1.0 dex. The solar-metallicity field dwarf sequence more or less follows the trend of the two sets of models.

Both the LOWZ and the SONORA models predict bluer $W1 - W2$ colours and redder $J - W2$ colours for lower metallicity objects in the 500–1000 K temperature range. This is clear for the Accident, since it has a significantly bluer $W1 - W2$ colour and a redder $J - W2$ colour than field Y dwarfs. For the rest of metal-poor T dwarf candidates, they do not tend to concentrate in a smaller $W1 - W2$ interval.

The LOWZ model predicts a $z_{PS1} - W1$ colour between 4 mag to 5.5 mag for objects between 500 K and 1600 K (black line in Fig. 3). The LOWZ models predict that for low metallicity (-2.0 dex) the temperature gradient is mainly responsible for the redward shift of the $z_{PS1} - W1$ colour from 4 to 5 mag. The SONORA model predicts a much stronger temperature dependence than the LOWZ model. The SONORA model also predicts a stable $z_{PS1} - W1$ colour for hotter objects no matter the metallicity, which contradicts the observations.

In the left panel of Fig. 3 and 4, the metal-poor objects segregate into three groups of different $z_{PS1} - W1$ colours with decreasing metallicity, tentatively named by as Group I, II, and III by Zhang et al. (2023). We infer that the LOWZ models underestimate the suppression of the z_{PS1} -band flux, caused by the

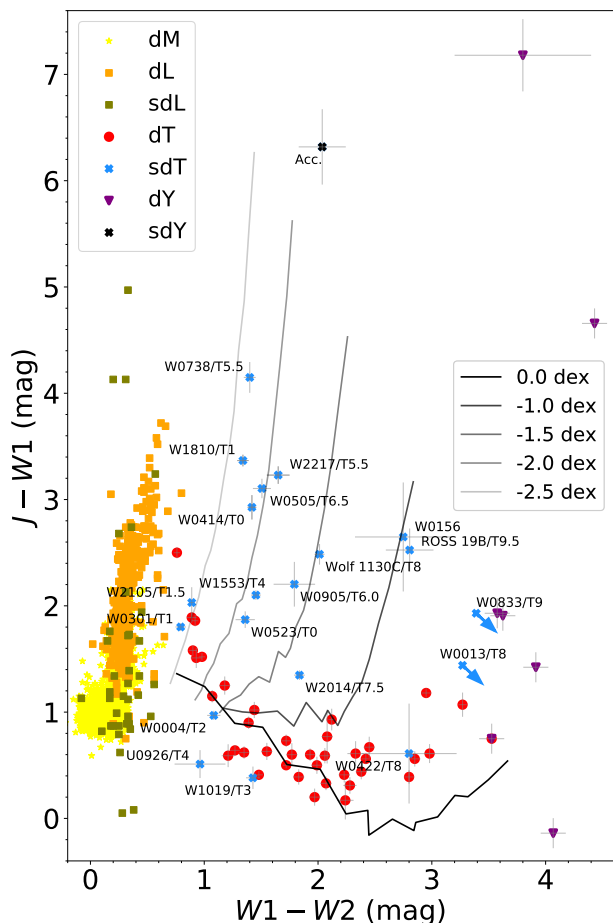


Fig. 5: $W1 - W2$ vs $J - W1$ colour-colour diagrams of all metal-poor T dwarf candidates (blue crosses and arrows) in Table 1 and in Zhang et al. (2023); and the Accident (the black cross and arrow). We also included solar-metallicity M, L, and T sequences from Pan-STARRS as yellow stars, orange squares, and red dots, respectively, along with L subdwarfs (olive squares), four Y0 dwarf, a Y2 dwarf, the Y4 dwarf (purple triangles), and a T9+Y0 system (red dot mixed with purple triangle). Error bars are included for all sources, except for M and L dwarfs. We also show five iso-metallicity curves from the low-metallicity theoretical model LOWZ with parameters $\log(g) = 5.0$, $\log_{10} K_{zz} = 2$, solar C/O ratio 0.55. From left to right of the five curves, the effective temperatures of the model decrease from 1600 K to 500 K, with a step of 100 K and 50 K above and under 1000K, respectively.

low metallicity; and also does the SONORA models, but only for hotter objects or early-T dwarfs.

On the other hand, the behaviour of the $z_{PS1} - W1$ colour of subdwarfs is similar to that of the $J - W1$ colour. Unlike the $z_{PS1} - W1$ vs. $W1 - W2$ diagram, the observations agree with model predictions in the $J - W1$ vs. $W1 - W2$ diagram (we only plot the LOWZ models in Fig. 5). The LOWZ and SONORA models predict that the $J - W1$ colours get significant redder for objects cooler than about 1000 K when metallicity decreases, and the temperature is the main driver for the metal-poor objects to have the $J - W1$ colours shifted redward. However, the hotter end of both models (1300–1600 K) exhibits the same problem in the $J - W1$ colours as in $z_{PS1} - W1$. They also do not accurately reproduce the observed L subdwarfs, as well as the extreme cold solar-metallicity Y2 and Y4 dwarfs. Solar-metallicity T dwarfs

exhibit greater dispersion across the spectral type in the $J - W1$ colour (around 2 mag) compare to the $z_{PS1} - W1$ colour (around 1.5 mag). This increased dispersion makes Group II harder to distinguish (the intermediate-metal-poor T dwarf group). In Fig. 5, the spectral types of each metal-poor object are shown, but no clear temperature gradient is evident.

3.3. $z_{PS1} - W1$ colour vs metallicity

To see the $z_{PS1} - W1$ colour trend against the metallicity more clearly, we assigned a coarse metallicity value to each source in our sample. With the exception of Wolf 1130C and Ross 19B, which have spectroscopically determined metallicities derived from their M dwarf primaries, the metallicities of the remaining objects are estimated based on metallicity subclass classifications obtained through spectroscopy or photometry. This classification of subdwarfs has been a long debated topic and it has not been fully established for T subdwarfs yet because of lack of objects across the whole spectral type range. We adopted the maximum interval of the metallicity value for subclasses published by different research groups for M and L subdwarfs (Gizis et al. 1997; Lépine et al. 2007; Zhang et al. 2017; Lodieu et al. 2019): i.e., subdwarfs have metallicities mainly between -0.3 and -1.0 dex, extreme subdwarfs between -1.0 and -1.7 dex, and ultra subdwarfs have below -1.7 dex. We also adopted a metallicity range of $+0.3$ to -0.3 dex for solar-metallicity field T/Y dwarfs.

For each individual object, we assign a corresponding metallicity based on the arguments below. A summary of the adopted metallicity for each object is given in Table 7.

- For the secondaries of comoving pairs, we assumed that all components of a multiple system have a similar chemical composition. There are different measurement of metallicity of the primary Wolf 1130A: -0.62 ± 0.10 dex (Wolf & Wallerstein 2006), -0.70 ± 0.12 dex (Mace et al. 2018), -0.64 ± 0.17 dex (Rojas-Ayala et al. 2012) but updated to -1.22 ± 0.24 dex (Newton et al. 2014). We adopted a maximum $1-\sigma$ range from -0.52 to 1.46 dex for Wolf 1130C.
- We adopted the iron abundance $[\text{Fe}/\text{H}]$ of the primary Ross 19A (-0.40 ± 0.12 dex; Schneider et al. 2021) for Ross 19B.
- Greco et al. (2019) used NIR spectroscopy and classified W0004, W0301, W1019 as subdwarfs. They do not appear as very metal-poor objects and they are not subluminous in the colour-magnitude diagrams in Fig. 2. We assigned them a metallicity $[\text{Fe}/\text{H}]$ from -0.3 to -1.0 dex. Meisner et al. (2020b) classified W0422 and W2207 as subdwarfs but did not specify the metal class. Hence, we adopted a possible range from normal subdwarfs to extreme subdwarfs from -0.3 to -1.7 dex for these two objects.
- Brooks et al. (2022) listed W0505 as an extreme T subdwarf based on its infrared colours, hence, we adopted a metallicity from -1.0 to -1.7 dex.
- Meisner et al. (2021) reported a spectral analysis for W1553, but different models provided different metallicity values, from -0.5 dex to ≤ -1.5 dex. We adopted that range.
- Meisner et al. (2023c) assigned W0156 a metallicity between -0.4 to -0.5 dex because of the adjacent locus to the Ross 19B and the LOWZ model track of -0.5 dex in the colour space. We adopted the same metallicity as that of Ross 19B.
- For WISEA J041451.67–585456.7, we adopted a range of metallicities from -0.5 to -1.5 dex (Schneider et al. 2020).

Table 7: Adopted metallicity [Fe/H] ranges for metal-poor T/Y dwarf candidates. Objects are ordered by RA. The ‘Spec.’ column indicates whether the object has been spectroscopically observed. The ‘Sublum.’ column indicates if the object appears subluminal in the colour-magnitude diagrams in Fig. 2.

Name	[Fe/H] _{max}	[Fe/H] _{min}	Spec.	Sublum.
T, Y dwarfs	+0.3	-0.3	-	-
W0004	-0.3	-1.0	Y	N
(1)W0013	-0.5	-1.5	N	-
W0156	-0.28	-0.52	N	-
W0301	-0.3	-1.0	Y	N
(2)Ross 19B	-0.28	-0.52	N	Y?
(3)W0414	-0.5	-1.5	Y	-
W0422	-0.3	-1.7	N	Y?
W0505	-1.0	-1.7	N	-
(4)W0523	-0.5	-1.5	N	-
W0711	-0.3	-1.0	Y	-
W0738	-0.5	-2.0	N	-
W0905	-0.3	-1.7	N	-
(1)W0833	-0.5	-1.5	N	-
ULAS0926	-0.3	-1.0	N	-
W1019	-0.3	-1.0	Y	-
(5)The Accident	-1.0	-	N	Y
(6)W1553	-0.5	-1.5	Y	Y
(7)W1810	-1.0	-2.0	Y	Y
Wolf 1130C	(8)-0.52	(9)-1.46	Y	Y
W2014	-0.3	-1.0	Y	Y?
W2105	0.0	-1.0	Y	-
W2207	-0.3	-1.7	N	-
W2217	-0.5	-2.0	N	Y

References. (1): Pinfield et al. (2014); (2): From the metallicity of the primary (Schneider et al. 2021); (3): Schneider et al. (2020); (4): Brooks et al. (2022); (5): Kirkpatrick et al. (2021b); (6): Meisner et al. (2021); (7): Lodieu et al. (2022); (8): From the metallicity of the primary (Woolf & Wallerstein 2006); (9) From the metallicity of the primary (Newton et al. 2014). Rest: from our assignation, see section 3.3.

For WISEA J181006.18–101000.5, we used the range derived by Lodieu et al. (2022), from -1.0 to -2.0 dex.

- Kellogg et al. (2018) classified W0711 as a subdwarf using its NIR spectrum, its low metallicity is consistent with the thick-disk or halo kinematics. We adopted the metallicity range of subdwarfs, from -0.3 to -1.0 dex.
- We classify W0738 and W2217 (Meisner et al. 2021) as extreme T subdwarfs based on their large motions and similar colours to the two known extreme T subdwarfs, W1810 and W0414. So we adopted the metallicity range of W1810 and W0414, i.e. from -0.5 to -2.0 dex for W0738 and W2217.
- For W0013 and W0833, Pinfield et al. (2014) estimated a metallicity range from -0.5 to -1.5 dex, based on their peculiar $H - W2$ colour.
- Murray et al. (2011) discussed the blue NIR colours and possible halo kinematics of ULAS0926, so we classify it as a subdwarf with a metallicity from -0.3 to -1.0 dex.
- W0905 and W2014 just falls outside the fiducial colour-colour criteria of extreme subdwarf region proposed by Meisner et al. (2023c). However, W2014 shows a normal spectrum in the Y -, J -, and H -bands. Only its K -band was suppressed (Mace et al. 2013a). Besides, W2014 appears inline with those T subdwarfs only in some of the colour-magnitude diagrams in Fig. 2, and has a $J - H$ colour ab-

normality. We hence assigned a wide metallicity range from subdwarf to extreme subdwarf to W0905, from -0.3 to -1.7 dex; but only a subdwarf metallicity to W2014, from -0.3 to -1.0 dex.

- The kinematics of W2105 shows that it could be a thick disk/halo dwarf, but the J - and H -band spectra do not show features of low metallicity (Luhman & Sheppard 2014), and Meisner et al. (2023c) excluded it from the list of extreme T subdwarf candidates because its colours put it outside of the locus where extreme T subdwarfs lie. Therefore, we adopted a metallicity from solar 0.0 dex to the most-metal-poor subdwarfs, -1.0 dex.

We plot the $z_{PS1} - W1$ colour and metallicity of solar-metallicity field T dwarfs and metal-poor T dwarf candidates in the left panel of Fig. 6. We highlighted objects with spectra as circles. We also plot the mean colour and the standard deviation of the colour of solar-metallicity field T dwarfs. First of all, the temperature effect for the solar-metallicity T dwarfs on this colour is less than 1 mag (from 4.5 to 5.5 mag). The metallicity groups I, II, III for the metal-poor T dwarfs, first introduced by Zhang et al. (2023), are now separated by the blue dashed lines in Fig. 3. We adopted $z_{PS1} - W1 = 5.5$ and 6.3 mag as the separation of groups I and II, and groups II and III, respectively. Group I is a mixture of solar-metallicity dwarfs and slightly-metal-poor subdwarfs, with similar $z_{PS1} - W1$ colours. The $z_{PS1} - W1$ colour does not change significantly at least until the metallicities of W0004, W0301, and W1019. Once the metallicity gets lower than ≈ -1.0 dex, the $z_{PS1} - W1$ colour shoots up and gets drastically redder.

We identify Ross 19B and W0156 as two outliers (dotted blue circles) of the Group III in the left panel of Fig. 6 with mildly low metallicities but unusually red $z_{PS1} - W1$ colours. Since the metallicity of W0156 was constrained by Ross 19B (Meisner et al. 2023c), it is not surprising that W0156 aligns with Ross 19B as an outlier. From this point forward, we will focus only on Ross 19B, although our conclusions are applicable to both objects.

Ignoring the possibility of wrong photometry, in the colour-magnitude diagrams, Ross 19B appears extremely subluminal compared to solar-metallicity T dwarf counterparts. It would likely be a colder object, a Y dwarf, which is not contradictory to the photometric spectral type determination: $T9.5 \pm 1.5$ (Schneider et al. 2021). We put both Ross 19B and W1056 into the right panel of Fig. 6, with the mean colour and the standard deviation of the colour of solar-metallicity field Y dwarfs, and the colour limit of the Accident. The colours of both Ross 19B and W1056 stay between the average colour of the solar-metallicity Y dwarfs and that of the Accident, which is consistent with their mildly low metallicities derived from Ross 19A.

Another possibility for the outlying of Ross 19B and W1056 could be having a lower metallicity than the value succeeded from Ross 19A, if they are very-late-T dwarfs. The absolute z_{PS1} magnitude difference between the solar-metallicity sequence and Ross 19B is larger than that between the solar-metallicity sequence and Wolf 1130C in Fig. 2. Wolf 1130C has a similar spectral type as Ross 19B. We therefore hypothesise that Ross 19B may have a much lower metallicity than Wolf 1130C, and certainly lower than its primary, Ross 19A. Ross 19 system has a projected separation of 9900 AU (Schneider et al. 2021). For such a loosely bounded system, it is hard for it to survive dynamically from the Galactic tides over its old age ($7.2^{+3.6}_{-3.2}$ Gyr; Schneider et al. 2021). For a binary with a semi-major axis 10000 au, the simulation for a system with total mass of $1M_{\odot}$

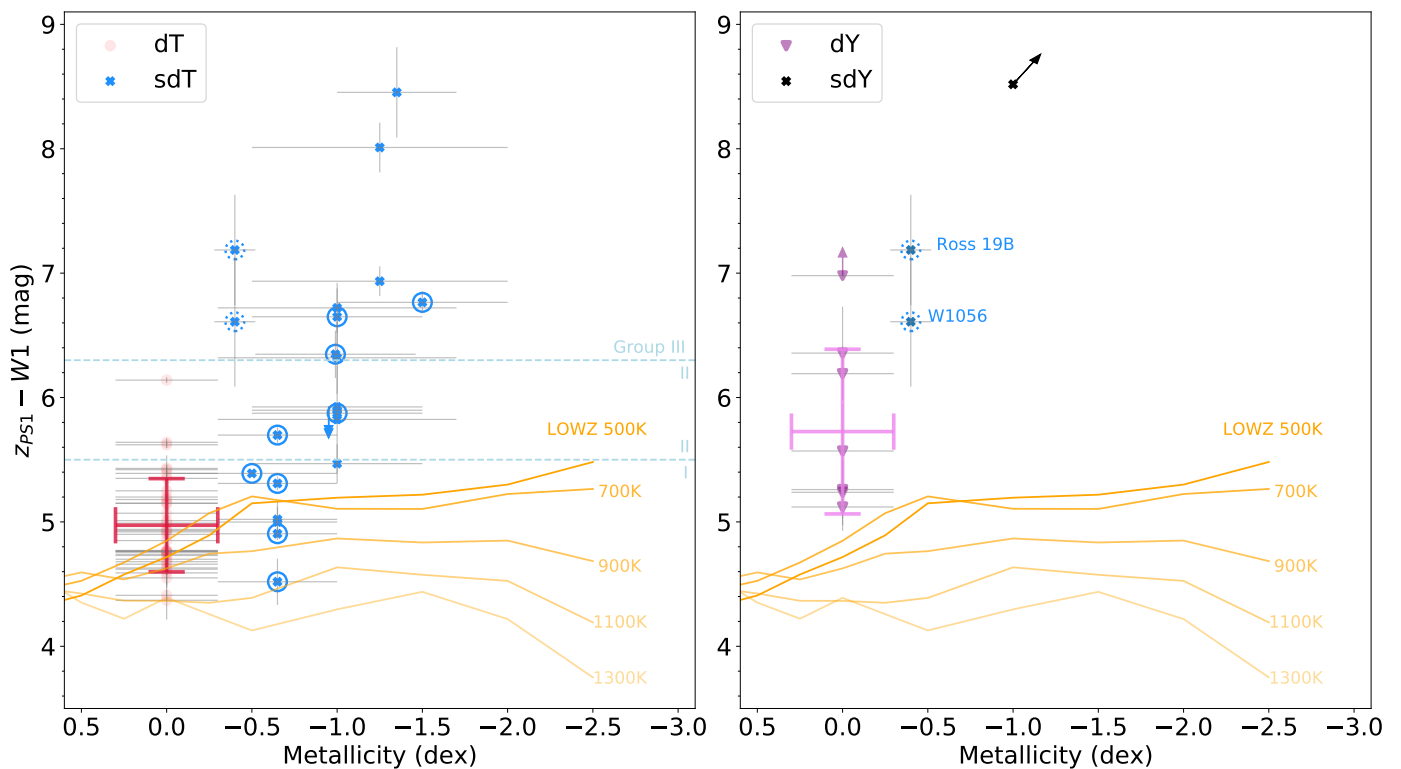


Fig. 6: $z_{PS1} - W1$ colour against metallicity for T and Y dwarfs. The vertical error bars are the photometric errors and the horizontal bars are the adopted metallicity ranges (Table 7). The blue and black crosses are metal-poor T and Y dwarf candidates, respectively. Some upper limit arrows are plotted next to the points to avoid overlapping. The solid blue circle indicates that the object has an NIR spectrum. The two very-late-type metal-poor T dwarf candidates or possible metal-poor Y dwarf candidates Ross 19B and W1056 are indicated by dotted blue circles and are plotted in both panels. The thick red and purple crosses demonstrate the average $z_{PS1} - W1$ value and dispersion of solar-metallicity T and Y dwarfs, respectively. We drew two blue dashed lines in the left panel at $z_{PS1} - W1 = 5.5$ and 6.3 mag to indicate the separation of Group I, II, and III in Fig. 3 for metal-poor T dwarfs. Five isothermal curves from 500 K to 1300 K from LOWZ model with parameters $\log(g) = 5.0$, $\log_{10} K_{zz} = 2$, C/O ratio of 0.55 are shown in orange colour.

yields a very low probability of surviving for 7 Gyr (Weinberg et al. 1987). We note that the Ross 19 system has only $0.4M_{\odot}$. The possibility of evolving from different systems and not sharing the same chemical abundance is not low for Ross 19AB. However, the chance for a metal-poor M dwarf catching specifically a brown dwarf with even lower metallicity is not high either. In summary, Ross 19B and W1056 are more likely to be colder objects, and they are among the metal-poor Y dwarf candidates.

Putting these two outliers aside, in the left panel of Fig. 6, we see that Group III with $z_{PS1} - W1 \geq 6.3$ mag contains objects with metallicity lower or equal than -1.0 dex, i.e., extreme subdwarfs. Their spectral types spread from T0 to T8. In other words, the $z_{PS1} - W1$ colour is observationally a good extreme subdwarf indicator for T dwarfs, which was first proposed by Zhang et al. (2023). This colour could be a metallicity indicator for Y dwarfs according to the right panel of Fig. 6 after adding Ross 19B and W1056, but more observations are needed to confirm this hypothesis.

We again plot the LOWZ models in both panels of Fig. 6, using five isothermal lines with metallicity from $+0.5$ dex to -2.5 dex. The LOWZ models do predict that the $z_{PS1} - W1$ colour gets redder with decreasing metallicity until -1.0 dex for objects cooler than 900 K (equivalent to mid- to late-T dwarfs). As the temperature decreases, the colour becomes redder in a more

pronounced manner. However, the models fail to account for the very red colours observed at lower metallicities for both T and early-Y dwarfs (objects with temperature higher than 500 K).

Our previous work attributed the redder $z_{PS1} - W1$ colours to the flux increase in the W1 band, due to the weakening of the methane absorption, and expected a saturation at some point Zhang et al. (2023). However, at this moment we still do not appreciate any sign of saturation in the $z_{PS1} - W1$ colour, although in the case of the current most metal-poor T dwarf with spectroscopic metallicity, W1810, methane is absent or very weak (Lodieu et al. 2022). On the other hand, the absorption wings of alkali metals, especially the sodium NaI and potassium KI resonance doublets at optical wavelengths are broadened in high-gravity atmospheres due to the collision with helium He and molecular hydrogen H_2 , contributing partly to the suppressed flux in the z passband (Burrows & Volobuyev 2003; Pavlenko et al. 2007; Allard et al. 2016; Phillips et al. 2020). This absorption could be even strengthened due to higher gravity and denser atmospheres in metal-poor environment (Allard et al. 2003, 2023, 2024). These two effects could be underestimated by the LOWZ model, explaining the current discrepancy with the observations.

We further checked the temperature dependence of the $z_{PS1} - W1$ colour. We plotted the colour of all objects against their spectral type in Fig. 7. We see that the $z_{PS1} - W1$ colour gets bluer

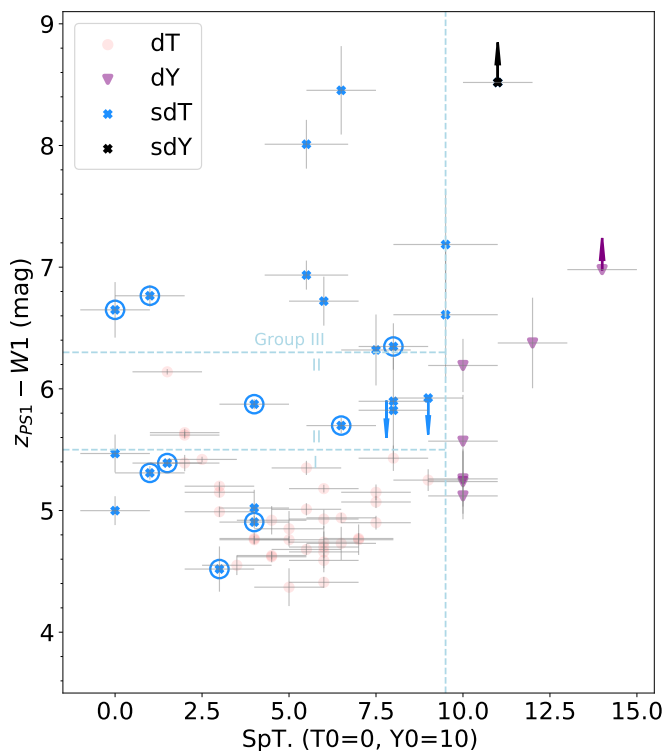


Fig. 7: $z_{PS1} - W1$ colour against spectral type. The solid blue circle indicates that the object has an NIR spectrum. All the objects have a spectral type uncertainty of one subtype, unless specified differently in Table 1. W0156 was classified as a T subdwarf without a subtype, we assigned it with the same late spectral type as Ross 19B. We assigned a Y0–Y2 range for the Accident, according to its effective temperature. T dwarfs are separated into three groups, and Group III are supposed to be the most metal-poor T dwarfs. The $z_{PS1} - W1$ colours of Group III dwarfs show no dependence on the spectral type.

until mid-T dwarfs and then gets redder for solar-metallicity dwarfs. The range of colours remains in a small interval between 4.5 mag to 5.5 mag. We do not see a clear spectral type dependence for Group III objects, and we can conclude that the differences in the effective temperature of solar-metallicity T dwarfs will not lead to an extreme red $z_{PS1} - W1$ colour. Thus, the $z_{PS1} - W1$ colour can reliably serve as an indicator for extreme T subdwarfs.

3.4. Most metal-poor objects

We see that W0505 and W0738 have exceptionally red $z_{PS1} - W1$ colours of 8.01 mag and 8.45 mag, respectively. There may exist a Group IV in the colour-colour diagram with $z_{PS1} - W1$ colours redder than 8.0 mag, represented by ultra subdwarfs (usdT) with metallicity $[Fe/H]$ below -1.7 dex. However, the WISE photometry of W0505 could be slightly affected by faint background sources, hence the true $z_{PS1} - W1$ colour of W0505 could be slightly bluer.

The Accident’s extreme low luminosity also points towards a very low effective temperature. The Accident has the reddest $z_{PS1} - W1$ colour among all the coldest subdwarf candidates, and a blue $W1 - W2$ colour suggesting that it could have a very low metallicity. Martín et al. (2024) observed a sharp transition towards bluer $z - J$ colours from 5 to 2 mag from late-T to Y2

dwarfs, respectively, as seen in the colour-magnitude diagram in Fig. 2. The transition agrees with the SONORA solar-metallicity model (Marley et al. 2021). We attribute this effect to the weakening of the very broad KI resonance doublet in the Y dwarf atmosphere, with alkali elements being locked into molecules at low temperatures (Lodders 1999) and carried into deeper layers by rain-out processes (Burrows & Sharp 1999). The Accident has a lower limit of 2.2 mag on its $z_{PS1} - J$, which is consistent with those of solar-metallicity Y dwarfs at the moment.

4. Conclusions

We obtained ground-based trigonometry parallaxes for five metal-poor T dwarf candidates and complemented them with those from the literature. We acquired z -band photometry for another 12 metal-poor T dwarf candidates and five-band optical photometry for the Accident, the only metal-poor Y dwarf candidate to date.

We demonstrated the subdwarf nature of W1553, W1810, Wolf 1130C, W2217, the Accident, and possibly Ross 19B, W0422, and W2014 using their loci in the optical-to-infrared colour-magnitude diagrams comparing with their solar-metallicity counterparts. We argue that W0004, and W0301 are not so metal-poor or they could be binary candidates based on their loci on the solar-metallicity sequence in the colour-magnitude diagrams. It is worthwhile to take an observation with adaptive optics or interferometry to spatially resolve these binary candidates.

We provided updated optical-IR colour-colour diagrams, effectively doubling the size of the previous metal-poor T dwarf sample. We strengthened our previous discovery about the relation between the low metallicity and the red $z_{PS1} - W1$ colour for T dwarfs, and possibly extended it to Y dwarfs, which is not predicted by the state-of-art models. Combining the three colours $z_{PS1} - W1$, $J - W1$, and $W1 - W2$ may break the metallicity-temperature degeneracy for the coldest populations, and is useful to identify future extreme- or even ultra- metal-poor T and Y dwarfs. We confirmed the candidacy of W0505 and W0738 to the population of extreme-metal-poor T dwarfs, and we propose that Ross 19B and W1056 could be Y subdwarf candidates.

We claim that NIR spectroscopy is essential to determine the metallicity of the extreme T subdwarf candidates W2217, W0505, and W0738 and . However, due to their faintness, this remains challenging with current ground-based instrumentation but could be achievable from space using the JWST. A more practical approach would be obtaining K -band photometry for W0505 and W2217. We also discuss the importance of the spectroscopic determination of the metallicity and temperature of Ross 19B as another benchmark object and an additional anchor point in the diagrams presented in this work. The analysis of the JWST spectrum of the Accident (programme GO 3558, PI A. Meisner; Meisner et al. 2023a) is of extreme importance since it could let us to synthesise the z_{PS1} photometry of the only Y subdwarf candidate, and measure its metallicity and other physical parameters.

In the current/future deep optical surveys like the ESA *Euclid* mission, Vera Rubin LSST and Roman space mission, we could launch a tailored survey to search for a specific ultracool population with a given metallicity and effective temperature (Solano et al. 2021; Martín et al. 2021). The main objective is to increase the samples of metal-poor T and Y dwarfs taking advantage of the complementarity between optical and NIR photometry, as well as astrometric measurements thanks to the repeated observations of Vera Rubin LSST and the *Euclid* deep fields.

Acknowledgements. Funding for this research was provided by the Agencia Estatal de Investigación del Ministerio de Ciencia e Innovación (AEI-MCINN) under grants PID2019-109522GB-C53 and PID2022-137241NB-C41 as well as the European Union (ERC, SUBSTELLAR, project number 101054354). BG acknowledges support from the Polish National Science Center (NCN) under SONATA grant No. 2021/43/D/ST9/0194. Based on observations made with the Gran Telescopio Canarias (GTC), installed at the Spanish Observatorio del Roque de los Muchachos of the Instituto de Astrofísica de Canarias, on the island of La Palma. This work is partly based on data obtained with the instrument HiPERCAM, built by the Universities of Sheffield, Warwick and Durham, the UK Astronomy Technology Centre, and the Instituto de Astrofísica de Canarias. Development of HiPERCAM was funded by the European Research Council, and its operations and enhancements by the Science and Technology Facilities Council. This work is partly based on data obtained with the instrument OSIRIS, built by a Consortium led by the Instituto de Astrofísica de Canarias in collaboration with the Instituto de Astronomía of the Universidad Autónoma de México. OSIRIS was funded by GRANTECAN and the National Plan of Astronomy and Astrophysics of the Spanish Government. This work is partly based on data obtained with the instrument EMIR, built by a Consortium led by the Instituto de Astrofísica de Canarias. EMIR was funded by GRANTECAN and the National Plan of Astronomy and Astrophysics of the Spanish Government. Based on observations collected at Centro Astronómico Hispano en Andalucía (CAHA) at Calar Alto, operated jointly by Instituto de Astrofísica de Andalucía (CSIC) and Junta de Andalucía. Based on observations collected at the European Southern Observatory under ESO programme 113.2688. This research has made use of the Spanish Virtual Observatory (<https://svo.cab.inta-csic.es>) project funded by MCIN/AEI/10.13039/501100011033/ through grant PID2020-112949GB-I00. This research has made use of the SVO Filter Profile Service "Carlos Rodrigo", funded by MCIN/AEI/10.13039/501100011033/ through grant PID2020-112949GB-I00. This research has made use of data provided by Astrometry.net. This research has made use of the Simbad and VizieR databases, and the Aladin sky atlas operated at the centre de Données Astronomiques de Strasbourg (CDS), and of NASA's Astrophysics Data System Bibliographic Services (ADS). This research has made use of the NASA/IPAC Infrared Science Archive, which is funded by the National Aeronautics and Space Administration and operated by the California Institute of Technology. This work has used the Pan-STARRS1 Surveys (PS1) and the PS1 public science archive that have been made possible through contributions by the Institute for Astronomy, the University of Hawaii, the Pan-STARRS Project Office, the Max-Planck Society and its participating institutes, the Max Planck Institute for Astronomy, Heidelberg and the Max Planck Institute for Extraterrestrial Physics, Garching, The Johns Hopkins University, Durham University, the University of Edinburgh, the Queen's University Belfast, the Harvard-Smithsonian Center for Astrophysics, the Las Cumbres Observatory Global Telescope Network Incorporated, the National Central University of Taiwan, the Space Telescope Science Institute, the National Aeronautics and Space Administration under Grant No. NNX08AR22G issued through the Planetary Science Division of the NASA Science Mission Directorate, the National Science Foundation Grant No. AST-1238877, the University of Maryland, Eotvos Lorand University (ELTE), the Los Alamos National Laboratory, and the Gordon and Betty Moore Foundation. This publication makes use of data products from the Wide-field Infrared Survey Explorer, which is a joint project of the University of California, Los Angeles, and the Jet Propulsion Laboratory/California Institute of Technology, funded by the National Aeronautics and Space Administration. This project used public archival data from the Dark Energy Survey (DES). Funding for the DES Projects has been provided by the U.S. Department of Energy, the U.S. National Science Foundation, the Ministry of Science and Education of Spain, the Science and Technology Facilities Council of the United Kingdom, the Higher Education Funding Council for England, the National Center for Supercomputing Applications at the University of Illinois at Urbana-Champaign, the Kavli Institute of Cosmological Physics at the University of Chicago, the Center for Cosmology and Astro-Particle Physics at the Ohio State University, the Mitchell Institute for Fundamental Physics and Astronomy at Texas A&M University, Financiadora de Estudos e Projetos, Fundação Carlos Chagas Filho de Amparo à Pesquisa do Estado do Rio de Janeiro, Conselho Nacional de Desenvolvimento Científico e Tecnológico and the Ministério da Ciência, Tecnologia e Inovação, the Deutsche Forschungsgemeinschaft and the Collaborating Institutions in the Dark Energy Survey. The Collaborating Institutions are Argonne National Laboratory, the University of California at Santa Cruz, the University of Cambridge, Centro de Investigaciones Energéticas, Medioambientales y Tecnológicas-Madrid, the University of Chicago, University College London, the DES-Brazil Consortium, the University of Edinburgh, the Eidgenössische Technische Hochschule (ETH) Zürich, Fermi National Accelerator Laboratory, the University of Illinois at Urbana-Champaign, the Institut de Ciències de l'Espai (IEEC/CSIC), the Institut de Física d'Altes Energies, Lawrence Berkeley National Laboratory, the Ludwig-Maximilians Universität München and the associated Excellence Cluster Universe, the University of Michigan, the National Optical Astronomy Observatory, the University of Nottingham, The Ohio State University, the OzDES Membership Consortium, the University of Pennsylvania, the University

of Portsmouth, SLAC National Accelerator Laboratory, Stanford University, the University of Sussex, and Texas A&M University. The national facility capability for SkyMapper has been funded through ARC LIEF grant LE130100104 from the Australian Research Council, awarded to the University of Sydney, the Australian National University, Swinburne University of Technology, the University of Queensland, the University of Western Australia, the University of Melbourne, Curtin University of Technology, Monash University and the Australian Astronomical Observatory. SkyMapper is owned and operated by The Australian National University's Research School of Astronomy and Astrophysics. The survey data were processed and provided by the SkyMapper Team at ANU. The SkyMapper node of the All-Sky Virtual Observatory (ASVO) is hosted at the National Computational Infrastructure (NCI). Development and support of the SkyMapper node of the ASVO has been funded in part by Astronomy Australia Limited (AAL) and the Australian Government through the Commonwealth's Education Investment Fund (EIF) and National Collaborative Research Infrastructure Strategy (NCRIS), particularly the National eResearch Collaboration Tools and Resources (NeCTAR) and the Australian National Data Service Projects (ANDS). This work made use of Astropy:³ a community-developed core Python package and an ecosystem of tools and resources for astronomy (Astropy Collaboration et al. 2013, 2018, 2022).

References

- Abbott, T. M. C., Abdalla, F. B., Allam, S., et al. 2018, *ApJS*, 239, 18
 Abbott, T. M. C., Adamów, M., Aguena, M., et al. 2021, *ApJS*, 255, 20
 Allard, N. F., Allard, F., Hauschildt, P. H., Kielkopf, J. F., & Machin, L. 2003, *A&A*, 411, L473
 Allard, N. F., Kielkopf, J. F., Myneni, K., & Blakely, J. N. 2024, *A&A*, 683, A188
 Allard, N. F., Myneni, K., Blakely, J. N., & Guillon, G. 2023, *A&A*, 674, A171
 Allard, N. F., Spiegelman, F., & Kielkopf, J. F. 2016, *A&A*, 589, A21
 Appenzeller, I., Fricke, K., Fürting, W., et al. 1998, *The Messenger*, 94, 1
 Astropy Collaboration, Price-Whelan, A. M., Lim, P. L., et al. 2022, *ApJ*, 935, 167
 Astropy Collaboration, Price-Whelan, A. M., Sipőcz, B. M., et al. 2018, *AJ*, 156, 123
 Astropy Collaboration, Robitaille, T. P., Tollerud, E. J., et al. 2013, *A&A*, 558, A33
 Bailer-Jones, C. A., Bizenberger, P., & Storz, C. 2000, in *Society of Photo-Optical Instrumentation Engineers (SPIE) Conference Series*, Vol. 4008, *Optical and IR Telescope Instrumentation and Detectors*, ed. M. Iye & A. F. Moorwood, 1305–1316
 Baumeister, H., Bizenberger, P., Bayler-Jones, C. A. L., et al. 2003, in *Society of Photo-Optical Instrumentation Engineers (SPIE) Conference Series*, Vol. 4841, *Instrument Design and Performance for Optical/Infrared Ground-based Telescopes*, ed. M. Iye & A. F. M. Moorwood, 343–354
 Beamín, J. C., Ivanov, V. D., Bayo, A., et al. 2014, *A&A*, 570, L8
 Best, W. M. J., Liu, M. C., Magnier, E. A., & Dupuy, T. J. 2020, *AJ*, 159, 257
 Best, W. M. J., Liu, M. C., Magnier, E. A., & Dupuy, T. J. 2021, *AJ*, 161, 42
 Best, W. M. J., Magnier, E. A., Liu, M. C., et al. 2018, *ApJS*, 234, 1
 Brooks, H., Kirkpatrick, J. D., Caselden, D., et al. 2022, *AJ*, 163, 47
 Burgasser, A. J., Kirkpatrick, J. D., Brown, M. E., et al. 2002, *ApJ*, 564, 421
 Burgasser, A. J., Kirkpatrick, J. D., Burrows, A., et al. 2003a, *ApJ*, 592, 1186
 Burgasser, A. J., Kirkpatrick, J. D., Liebert, J., & Burrows, A. 2003b, *ApJ*, 594, 510
 Burgasser, A. J., Witte, S., Helling, C., et al. 2009, *ApJ*, 697, 148
 Burningham, B., Smith, L., Cardoso, C. V., et al. 2014, *MNRAS*, 440, 359
 Burrows, A. & Sharp, C. M. 1999, *ApJ*, 512, 843
 Burrows, A. & Volobuyev, M. 2003, *ApJ*, 583, 985
 Cepa, J., Aguiar-Gonzalez, M., Gonzalez-Escalera, V., et al. 2000, in *Optical and IR Telescope Instrumentation and Detectors*, Vol. 4008, *SPIE*, 623–631
 Chabrier, G., Baraffe, I., Phillips, M., & Debras, F. 2023, *A&A*, 671, A119
 Chambers, K. C., Magnier, E. A., Metcalfe, N., et al. 2016, *arXiv e-prints*, arXiv:1612.05560
 Cushing, M. C., Kirkpatrick, J. D., Gelino, C. R., et al. 2011, *ApJ*, 743, 50
 Cushing, M. C.,Looper, D., Burgasser, A. J., et al. 2009, *ApJ*, 696, 986
 Cutri, R. M., Skrutskie, M. F., van Dyk, S., et al. 2003, *2MASS All Sky Catalog of point sources*.
 Delorme, P., Delfosse, X., Albert, L., et al. 2008, *A&A*, 482, 961
 Dhillon, V. S., Bezawada, N., Black, M., et al. 2021, *MNRAS*, 507, 350
 Freudling, W., Romaniello, M., Bramich, D. M., et al. 2013, *A&A*, 559, A96
 Gizis, J. E., Scholz, R. D., Irwin, M., & Jahreiss, H. 1997, *MNRAS*, 292, L41
 Goodman, S. J. 2021, *Research Notes of the American Astronomical Society*, 5, 178

³ <http://www.astropy.org>

- Greco, J. J., Schneider, A. C., Cushing, M. C., Kirkpatrick, J. D., & Burgasser, A. J. 2019, *AJ*, 158, 182
- Kellogg, K., Kirkpatrick, J. D., Metchev, S., Gagné, J., & Faherty, J. K. 2018, *AJ*, 155, 87
- Kirkpatrick, J. D., Gelino, C. R., Cushing, M. C., et al. 2012, *ApJ*, 753, 156
- Kirkpatrick, J. D., Gelino, C. R., Faherty, J. K., et al. 2021a, *ApJS*, 253, 7
- Kirkpatrick, J. D., Marocco, F., Caselden, D., et al. 2021b, *ApJ*, 915, L6
- Kirkpatrick, J. D., Martin, E. C., Smart, R. L., et al. 2019, *ApJS*, 240, 19
- Kirkpatrick, J. D., Schneider, A., Fajardo-Acosta, S., et al. 2014, *ApJ*, 783, 122
- Kovács, Z., Mall, U., Bizenberger, P., Baumeister, H., & Röser, H.-J. 2004, in *Society of Photo-Optical Instrumentation Engineers (SPIE) Conference Series*, Vol. 5499, *Optical and Infrared Detectors for Astronomy*, ed. J. D. Garnett & J. W. Beletic, 432–441
- Kuchner, M. J., Faherty, J. K., Schneider, A. C., et al. 2017, *ApJ*, 841, L19
- Lang, D., Hogg, D. W., Mierle, K., Blanton, M., & Roweis, S. 2010, *AJ*, 139, 1782
- Leggett, S. K., Tremblin, P., Phillips, M. W., et al. 2021, *ApJ*, 918, 11
- Lépine, S., Rich, R. M., & Shara, M. M. 2007, *ApJ*, 669, 1235
- Liu, M. C., Dupuy, T. J., Bowler, B. P., Leggett, S. K., & Best, W. M. J. 2012, *ApJ*, 758, 57
- Lodders, K. 1999, *ApJ*, 519, 793
- Lodieu, N., Allard, F., Rodrigo, C., et al. 2019, *A&A*, 628, A61
- Lodieu, N., Béjar, V. J. S., & Rebolo, R. 2013, *A&A*, 550, L2
- Lodieu, N., Zapatero Osorio, M. R., Martín, E. L., Rebolo López, R., & Gauza, B. 2022, *A&A*, 663, A84
- Lodieu, N., Zapatero Osorio, M. R., Martín, E. L., Solano, E., & Aberasturi, M. 2010, *ApJ*, 708, L107
- Luhman, K. L. 2014, *ApJ*, 786, L18
- Luhman, K. L. & Sheppard, S. S. 2014, *ApJ*, 787, 126
- Luhman, K. L., Tremblin, P., Alves de Oliveira, C., et al. 2024, *AJ*, 167, 5
- Mace, G. N., Kirkpatrick, J. D., Cushing, M. C., et al. 2013a, *ApJS*, 205, 6
- Mace, G. N., Kirkpatrick, J. D., Cushing, M. C., et al. 2013b, *ApJ*, 777, 36
- Mace, G. N., Mann, A. W., Skiff, B. A., et al. 2018, *ApJ*, 854, 145
- Mainzer, A., Bauer, J., Cutri, R. M., et al. 2014, *ApJ*, 792, 30
- Marley, M. S., Saumon, D., Visscher, C., et al. 2021, *ApJ*, 920, 85
- Marocco, F., Eisenhardt, P. R. M., Fowler, J. W., et al. 2021, *ApJS*, 253, 8
- Martín, E. L., Zhang, J. Y., Esparza, P., et al. 2021, *A&A*, 655, L3
- Martín, E. L., Zhang, J. Y., Lanchas, H., et al. 2024, *A&A*, 686, A73
- Meisner, A., Bardalez Gagliuffi, D. C., Bejar, V., et al. 2023a, *The First Spectrum of the Coldest Halo Brown Dwarf, JWST Proposal. Cycle 2, ID. #3558*
- Meisner, A. M., Caselden, D., Kirkpatrick, J. D., et al. 2020a, *ApJ*, 889, 74
- Meisner, A. M., Caselden, D., Schlafly, E. F., et al. 2023b, *Research Notes of the American Astronomical Society*, 7, 36
- Meisner, A. M., Faherty, J. K., Kirkpatrick, J. D., et al. 2020b, *ApJ*, 899, 123
- Meisner, A. M., Leggett, S. K., Logsdon, S. E., et al. 2023c, *AJ*, 166, 57
- Meisner, A. M., Schneider, A. C., Burgasser, A. J., et al. 2021, *ApJ*, 915, 120
- Morganson, E., Gruendl, R. A., Menanteau, F., et al. 2018, *PASP*, 130, 074501
- Mukherjee, S., Fortney, J., Morley, C., et al. 2023a, *The Sonora Substellar Atmosphere Models. IV. Elf Owl: Atmospheric Mixing and Chemical Disequilibrium with Varying Metallicity and C/O Ratios (T-type Models)*
- Mukherjee, S., Fortney, J., Morley, C., et al. 2023b, *The Sonora Substellar Atmosphere Models. IV. Elf Owl: Atmospheric Mixing and Chemical Disequilibrium with Varying Metallicity and C/O Ratios (Y-type Models)*
- Mukherjee, S., Fortney, J. J., Morley, C. V., et al. 2024, *ApJ*, 963, 73
- Murray, D. N., Birmingham, B., Jones, H. R. A., et al. 2011, *MNRAS*, 414, 575
- Nakajima, T., Oppenheimer, B., Kulkarni, S., et al. 1995, *nature*, 378, 463
- Newton, E. R., Charbonneau, D., Irwin, J., et al. 2014, *AJ*, 147, 20
- Oke, J. B. 1974, *ApJS*, 27, 21
- Onken, C. A., Wolf, C., Bessell, M. S., et al. 2024, *arXiv e-prints*, arXiv:2402.02015
- Park, R. S., Folkner, W. M., Williams, J. G., & Boggs, D. H. 2021, *AJ*, 161, 105
- Pavlenko, Y. V., Zhukovska, S. V., & Volobuev, M. 2007, *Astronomy Reports*, 51, 282
- Phillips, M. W., Tremblin, P., Baraffe, I., et al. 2020, *A&A*, 637, A38
- Pinfield, D. J., Gomes, J., Day-Jones, A. C., et al. 2014, *MNRAS*, 437, 1009
- Rebolo, R., Osorio, M., & Martín, E. 1995, *Nature*, 377, 129
- Rodrigo, C. & Solano, E. 2020, in *XIV.0 Scientific Meeting (virtual) of the Spanish Astronomical Society*, 182
- Rodrigo, C., Solano, E., & Bayo, A. 2012, *SVO Filter Profile Service Version 1.0, IVOA Working Draft 15 October 2012*
- Rojas-Ayala, B., Covey, K. R., Muirhead, P. S., & Lloyd, J. P. 2012, *ApJ*, 748, 93
- Saumon, D., Bergeron, P., Lunine, J. I., Hubbard, W. B., & Burrows, A. 1994, *ApJ*, 424, 333
- Schneider, A. C., Burgasser, A. J., Gerasimov, R., et al. 2020, *ApJ*, 898, 77
- Schneider, A. C., Meisner, A. M., Gagné, J., et al. 2021, *ApJ*, 921, 140
- Sivarani, T., Lépine, S., Kembhavi, A. K., & Gupchup, J. 2009, *ApJ*, 694, L140
- Solano, E., Gálvez-Ortiz, M. C., Martín, E. L., et al. 2021, *MNRAS*, 501, 281
- Stetson, P. B. 1987, *PASP*, 99, 191
- Tody, D. 1986, in *Society of Photo-Optical Instrumentation Engineers (SPIE) Conference Series*, Vol. 627, *Instrumentation in astronomy VI*, ed. D. L. Crawford, 733
- Tody, D. 1993, in *Astronomical Society of the Pacific Conference Series*, Vol. 52, *Astronomical Data Analysis Software and Systems II*, ed. R. J. Hanisch, R. J. V. Brissenden, & J. Barnes, 173
- Weinberg, M. D., Shapiro, S. L., & Wasserman, I. 1987, *ApJ*, 312, 367
- Woolf, V. M. & Wallerstein, G. 2006, *PASP*, 118, 218
- Zhang, J. Y., Lodieu, N., & Martín, E. L. 2023, *A&A*, 678, A105
- Zhang, Z. H., Galvez-Ortiz, M. C., Pinfield, D. J., et al. 2018, *MNRAS*, 480, 5447
- Zhang, Z. H., Pinfield, D. J., Gálvez-Ortiz, M. C., et al. 2017, *MNRAS*, 464, 3040

Appendix A: GTC & VLT optical images of metal-poor T and Y dwarf candidates.

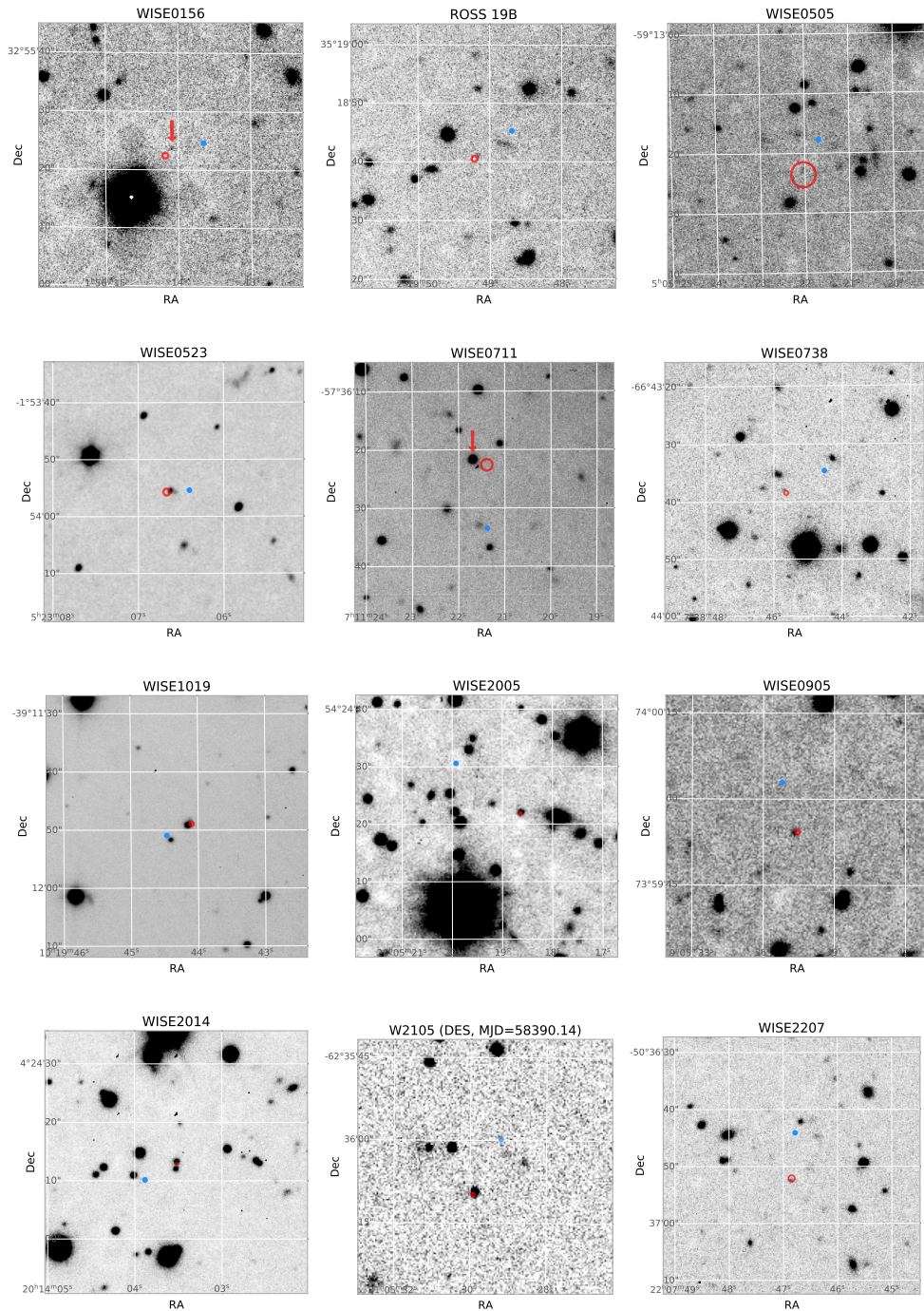


Fig. A.1: $45'' \times 45''$ DES, GTC/OSIRIS, and VLT/FORS2 z -band images of the fields of all the targets with conventional orientation (up is North and left is East). The blue dots are the object positions at the previous epochs published by other authors (Table 1), and the red ellipses are the projected positions where those targets are supposed to be on the dates of the observations according to their proper motions from the literature in Table 1. Parallax effects are negligible. The two semi-axes of the ellipses show the errors of projected position in RA and Dec, based on proper motion uncertainties and the time difference between the two epochs. All the objects have been detected. The correct positions of W0156 and W0711 are pointed out by red arrows.

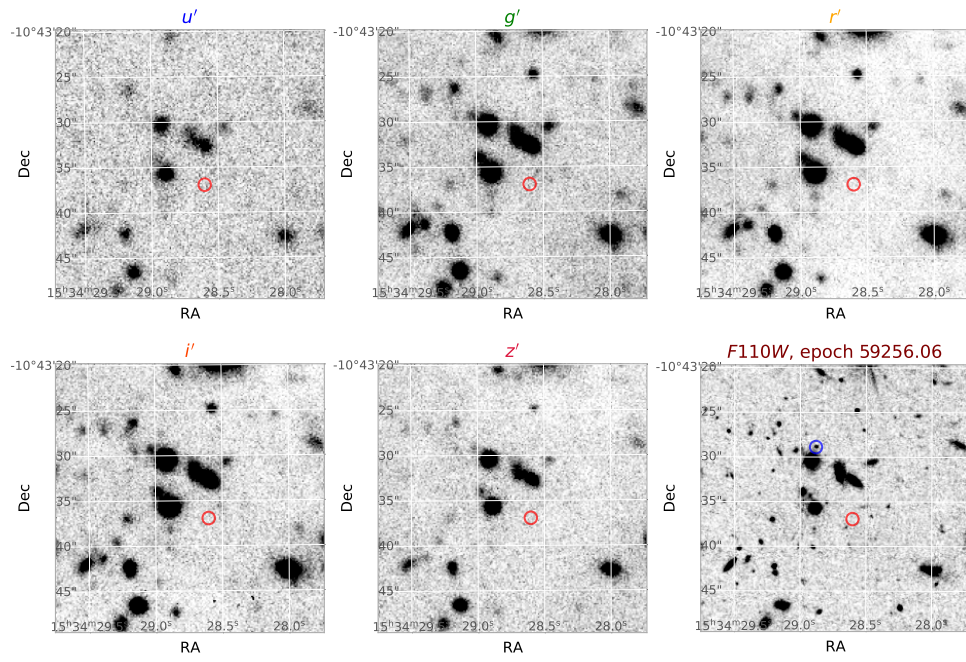


Fig. A.2: $30'' \times 30''$ GTC/HiPERCAM quintuple-band optical images of the Accident field with red circles indicating the expected position at the HiPERCAM epoch, compared with HST F110W image (right bottom) with blue circle indicating the Accident at the HST observation epoch. The Accident was not detected in any of the bands.